Radiative forcing by ~~super-volcano eruptions~~supereruptions

Eirik R. Enger[1], Rune Graversen[1], Audun Theodorsen[1]

[1]UiT The Arctic University of Norway, Tromsø, Norway

Key Points:

- The ~~linear RF dependence on AOD breaks down for eruptions larger than Mt. Pinatubo~~ ~~The RF~~ ERF to AOD ratio has a time-after-eruption dependence on eruption latitude.
- ~~Temperature and RF~~ No simulations across several climate models are found to produce ERF perturbations beyond $-65\,\mathrm{Wm}^{-2}$.
- Temperature and ERF peak values has a linear dependence ~~and reaches an upper limit~~ with maximum temperature perturbations of $\sim -10\,\mathrm{K}$.

Corresponding author: Eirik R. Enger, `eirik.r.enger@uit.no`

Abstract

Volcanic activity causes cooling of the climate due to reflection of solar radiation by associated aerosols. The climate effect of an eruption may last for about a decade, but where the climate effect is only loosely tied to the magnitude of the eruption. We investigate the climatic effects of volcanic eruptions spanning from Mt. Pinatubo-sized events to supereruptions. The study is based on ensemble simulations in the Community Earth System Model Version 2 (CESM2) climate model ~~using~~ applying the Whole Atmosphere Community Climate Model Version 6 (WACCM6) atmosphere model. Our analysis focuses on the impact of different SO_2-amount injections on stratospheric aerosol optical depth (AOD), effective radiative forcing (ERF), and global ~~temperature anomalies. Unlike the traditional linear models used for smaller eruptions, our results reveal a non-linear relationship between RF and AOD for larger eruptions. We also~~ mean surface temperature (GMST) anomalies. We uncover a notable time-dependent decrease in aerosol forcing efficiency (ERF normalised by AOD) across all eruption magnitudes during the first post-eruption year. In addition, ~~the study reveals that larger as compared to medium-sized eruption events produce a delayed and sharper peak in AOD, and a longer-lasting temperature response while the time evolution of RF remains similar between the two eruption types. When including the results of previous studies, we find that relating SO_2 to any other parameter is inconsistent across models compared to the relationships between AOD, RF, and temperature anomaly. Thus, we expect~~ it is revealed that the largest eruptions investigated in this study, including several previous supereruption simulations, produces peak ERF anomalies bounded at $-65\,\mathrm{Wm}^{-2}$. Further, we find a close linear relationship between peek GMST and ERF, effectively bounding the GMST anomaly to at most $\sim -10\,\mathrm{K}$. This is consistent across several previous studies using different climate models, while the largest uncertainty in model codes is found to relate to ~~Finally, we find that the peak RF approaches a limiting value, and that the peak temperature response follows linearly, effectively bounding the temperature anomaly to at most $\sim -12\,\mathrm{K}$~~the chemistry and physics of aerosol evolution.

Plain Language Summary

Volcanic eruptions can have a significant impact on the Earth's climate. ~~Eruptions large enoughthat~~ The gases from volcanic eruptions form aerosols. If the eruption is large enough, these aerosols may reach the stratosphere where they cause a cooling ~~effect~~ of the climate by reflecting sunlight. Typically, an eruption is ~~measured~~ distinguished by

its impact on the opacity of the stratosphere and the change in the energy balance at the top of the atmosphere when the surface temperature is held fixed. The two measures are often assumed to be linearly related, but the linearity is ~~tested only against eruptions~~ useful only for eruptions of sizes seen in the last two millennia. We use a coupled climate model to simulate the impact of eruptions of sizes up to the largest known eruptions. The smallest eruptions we simulate are still large enough to cause global climate effects. ~~We find a clear~~ In addition to the expected non-linear relationship ~~for eruptions larger than the ones seen in the past two millennia. Our simulations and supporting data shows that the eruption latitude significantly influences the development of the relationship~~ between energy imbalance and stratospheric opacity ~~with time after the eruption~~for larger and larger eruptions, the ratio is found to also change over time. Additionally, we find evidence that the peak energy imbalance reaches a limit, and that the peak temperature response follows linearly with the peak energy imbalance, also reaching a limiting value.

1 Introduction

~~Effective radiative forcing (RF) and stratospheric~~ Stratospheric aerosol optical depth (AOD) and effective radiative forcing (ERF) are crucial metrics ~~representing the~~ used to quantify the impact of major volcanic eruptions. The AOD represent the opacity of the stratosphere while ERF specifically is the energy imbalance at ~~top-of-the-atmosphere (TOA) and the stratospheric opacity due to aerosol scattering, respectively. They are extensively used to quantify the impact of major volcanic eruptions. The~~ the top-of-atmosphere when ocean and sea-ice is held fixed. Radiative forcing can however be calculated differently, and an agreed-upon methodology has thus not always existed (Forster et al., 2016). While ERF takes into account rapid adjustments, instantaneous radiative forcing (IRF) does not, with a third estimate of radiative forcing being a stratospherically adjusted radiative forcing where all surface and tropospheric conditions are kept fixed (Myhre et al., 2013; Forster et al., 2016). ERF, as used in this study, have been found to be the most precise indicator of the temperature response to a given forcing agent (Myhre et al., 2013; Forster et al., 2016), and a general assumption of a linear dependency of ~~RF~~ ERF on AOD is commonly adopted (Myhre et al., 2013; Andersson et al., 2015)~~, and applying~~. Applying such a linear relationship has yielded reasonably accurate estimates in climate model simulations of volcanic eruptions (Mills et al., 2017; Hansen, Nazarenko, et al., 2005; Gregory et al., 2016; Marshall et al., 2020; Pitari et al., 2016). Yet, a wide spread in the estimated aerosol forcing ef-

ficiencies (~~RF~~ ERF normalised by AOD) ~~exists~~ prevails among studies, spanning approximately from ~~$\sim -15\,\mathrm{Wm^{-2}AOD^{-1}}$ (Pitari et al., 2016) to (Myhre et al., 2013)~~$\sim -15\,\mathrm{Wm^{-2}}$ per unit AOD (hereafter $\mathrm{Wm^{-2}AOD^{-1}}$) (Pitari et al., 2016) to $\sim -25\,\mathrm{Wm^{-2}AOD^{-1}}$ (Hansen, Sato, et al., 2005). Additionally, these estimates are predominantly based on small eruptions with AOD values up to at most ~ 0.7.

Although H_2O, N_2, and CO_2 are the most abundant gases emitted by volcanoes (Robock, 2000), sulphur species such as SO_2 provide a comparatively greater influence due to the ~~comparatively high~~ higher background concentrations of the former gases in the atmosphere. The transformation of SO_2 molecules through reactions with OH and H_2O leads to the formation of sulphuric acid (H_2SO_4) ~~(Robock, 2000)~~(Pinto et al., 1989; Zhao et al., 1995), which scatters sunlight thereby elevating planetary albedo and reducing the ~~RF~~ERF. As the conversion from SO_2 to H_2SO_4 occurs over weeks (Pinto et al., 1989; Zhao et al., 1995), the peak ~~RF~~ H_2SO_4 burden experiences a slight delay from the eruption's peak SO_2 injection. The lifetime of the H_2SO_4 aerosols in the stratosphere depends on various factors, including aerosol size (Rampino & Self, 1982; Pinto et al., 1989; Marshall et al., 2019), latitude (Marshall et al., 2019; Toohey et al., 2019), volcanic plume height (Marshall et al., 2019), ~~aerosol size (Marshall et al., 2019),~~ the quasi-biennial oscillation phase (Pitari et al., 2016) and the season of the year (determining to which hemisphere aerosols are transported) (Toohey et al., 2011, 2019). In the case of tropical eruptions, aerosols are typically transported poleward in the stratosphere and descend back to mid-latitude troposphere within one to two years (Robock, 2000). Upon descending below the tropopause, these aerosols are readily removed by wet deposition (Liu et al., 2012).

Before the current era of significant anthropogenic climate forcing, volcanic eruptions were the primary forcing mechanism behind Earth's climate variability during the Holocene period (Schurer et al., 2013). Despite this substantial impact, few climate-model experiments have included volcanic forcing when simulating climate evolution during the Holocene (Sigl et al., 2022), likely implying an exaggerated positive forcing (Gregory et al., 2016; Solomon et al., 2011). This absence of persistent cooling is one of several factors that have been suggested to contribute to the common disparity between simulated and observed global warming (Andersson et al., 2015). Despite extensive attention on understanding the way volcanic eruptions influence climate, questions regarding aerosol particle processes—such as growth and creation rates when OH is scarce—remain unanswered ~~(e.g. Robock, 2000; Zanchettin et al., 2019; Marshall et al., 2020, 2022)~~(e.g. Zanchettin et al., 2019; Marshall et

. These processes impact aerosol scattering efficiency and potentially the ~~RF~~ ERF to AOD relationship. Marshall et al. (2020) observe higher aerosol forcing efficiency in post-eruption years 2 and 3 compared to year 1, and attribute this post-eruption increase in aerosol forcing efficiency to strong spatial concentration in the initial year and subsequent distribution of aerosols over a larger area. This spatial redistribution increases the albedo per global mean AOD thereby causing a stronger ~~RF~~ ERF to AOD ratio (Marshall et al., 2020).

Previous studies of both Mt. Pinatubo (Mills et al., 2017; Hansen, Nazarenko, et al., 2005) and volcanoes within the instrumental era (Gregory et al., 2016) have been used to estimate the relationship between the ~~RF~~ ERF energy imbalance and change in AOD~~caused by volcanic eruptions~~. While Myhre et al. (2013) employ a formula scaling ~~RF~~ ERF by AOD to obtain $-25\,\mathrm{Wm^{-2}AOD^{-1}}$, recent literature reports estimates ~~down to~~ as small as $-19.0 \pm 0.5\,\mathrm{Wm^{-2}AOD^{-1}}$ (Gregory et al., 2016) and $-18.3 \pm 1.0\,\mathrm{Wm^{-2}AOD^{-1}}$ (Mills et al., 2017). Synthetic volcano simulations in Marshall et al. (2020) yield a scaling factor of $-20.5 \pm 0.2\,\mathrm{Wm^{-2}AOD^{-1}}$ across an ensemble of 82 simulations featuring varying injection heights and latitudes of volcanic emissions, with injected SO_2 ranging from 10 to 100 $\mathrm{Tg(SO_2)}$.

A similar simulation setup, albeit with notable differences, was conducted by Niemeier and Timmreck (2015), involving an ensemble of 14 levels of injected sulphur spanning between $1\,\mathrm{Tg(S)yr^{-1}}$ ($2\,\mathrm{Tg(SO_2)yr^{-1}}$) and $100\,\mathrm{Tg(S)yr^{-1}}$ ($200\,\mathrm{Tg(SO_2)yr^{-1}}$). These geoengineering simulations maintained continuous sulphur injections, running until a steady sulphur level was achieved. Results indicated an inverse exponential relationship between ~~RF and injected SO_2~~ maximum forcing and annually injected SO_2, converging to $-65\,\mathrm{Wm^{-2}}$ (Eq. 1). Even the 100× Mt. Pinatubo ~~super-volcano~~ supereruption simulation by Jones et al. (2005), which obtained a peak ~~RF~~ ERF of $-60\,\mathrm{Wm^{-2}}$, is below the suggested limit of $-65\,\mathrm{Wm^{-2}}$. Moreover, Timmreck et al. (2010) find a peak ERF anomaly of $-18\,\mathrm{Wm^{-2}}$ from a 1700 $\mathrm{Tg(SO_2)}$ eruption simulation, which corresponds well with the function estimated by Niemeier and Timmreck (2015) at an annual injecting rate of 1700 $\mathrm{Tg(SO_2)yr^{-1}}$. Several studies have demonstrated a linear relationship of approximately $-20\,\mathrm{Wm^{-2}AOD^{-1}}$ between ~~RF~~ ERF and AOD, although substantial variability exists in the slope among studies (Mills et al., 2017; Hansen, Nazarenko, et al., 2005; Gregory et al., 2016; Marshall et al., 2020; Pitari et al., 2016). Moreover, a time-after-eruption dependence on the ~~RF~~ ERF to AOD ratio is found in Marshall et al. (2020), whereas Niemeier and Timmreck (2015) revealed a non-linear relationship between ~~RF~~ ERF and injected SO_2 rate.

Thus, a consensus on the relationship between injected SO_2, AOD, and ~~RF~~ ERF has yet to be established.

One avenue that has garnered considerable attention is comparing the magnitude of volcanic or volcano-like forcings to increased CO_2 levels. Several studies explore the connection between volcanic forcing and the climate sensitivity to a doubling of CO_2 (Boer et al., 2007; Marvel et al., 2016; Merlis et al., 2014; Ollila, 2016; Richardson et al., 2019; Salvi et al., 2022; Wigley et al., 2005). The comparison of forcing from volcanoes and CO_2 aims to mitigate the large uncertainty in estimates of the sensitivity of the real climate system. Inferring climate sensitivity from volcanic eruption events has been attempted as a way to constrain the sensitivity (Boer et al., 2007) by assuming that volcanic and CO_2 forcings produce similar feedbacks (Pauling et al., 2023). Earlier studies suggest the potential for constraining equilibrium cilmate sensitivity (ECS) using volcanoes (Bender et al., 2010), provided that ECS is constrained by ~~effective radiative forcing (ERF) rather than instantaneous radiative forcing (IRF)~~ERF rather than IRF, as ERF accounts for rapid atmospheric adjustments in contrast to IRF ~~(Richardson et al., 2019)~~(C. J. Smith et al., 2018; Richardson e
. However, other studies refute this approach, pointing out that different sensitivities of volcanic forcing and CO_2 doubling seem to exist (Douglass et al., 2006), or that constraining the ECS by ERF lacks accuracy due to the precision of climate simulations (Boer et al., 2007; Salvi et al., 2022). Although ERF offers a more suitable indicator of forcing than IRF (Marvel et al., 2016; Richardson et al., 2019), more recent studies conclude that ECS cannot be constrained from volcanic eruption events (Pauling et al., 2023).

Employing eruptions about an order of magnitude or more greater than the Mt. Pinatubo eruption (Volcano-Climate Index value greater than 3 (Schmidt & Black, 2022)) enhances the signal-to-noise ratio without necessitating an extensive and computationally expensive ensemble, and as such, is a tempting shortcut to try and mimic a large ensemble of smaller volcanic eruptions. However, the AOD, ~~RF, and temperature~~ ERF, and GMST signatures are not necessarily a simple scaling of that of smaller volcanic eruptions. Previous studies have simulated ~~super-volcanoes~~ supereruptions using AOD as the input forcing, where the AOD was that of Mt. Pinatubo scaled by a factor of one hundred (Jones et al., 2005). ~~This approach may~~ More recent studies find this approach will yield incorrect results, ~~both~~ because the peak of the AOD ~~may be too small or too big, but also because~~ is likely to be too large, and the evolution of the AOD could be inappropriate due to OH scarcity and aerosol size (Timmreck et al., 2009, 2010). Likewise, a different

AOD evolution may be found from similar size eruptions, but at different latitudes (Schneider et al., 2009; Marsha . To investigate ~~this issue,~~ the climate effects of large, Mt. Pinatubo-like, eruptions compared to supereruptions, as well as latitudinal effects, our simulations are based on four levels of injected SO_2 covering three orders of magnitude and the inclusion of one high latitude eruption of the second largest injected SO_2 case.

We conducted ensemble simulations of volcanic eruptions in the Community Earth System Model Version 2 (CESM2) coupled with the Whole Atmosphere Community Climate Model Version 6 (WACCM6). The ensembles span four different levels of injected SO_2: 26 Tg(SO_2), 400 Tg(SO_2), 1629 Tg(SO_2) and 3000 Tg(SO_2). Details regarding the experimental setup are provided in section 2. Our findings reveal non-linear ~~RF~~ ERF to AOD dependencies for ~~medium~~ large to super-volcano size eruptions. Additionally, we observe a time-dependent variation in the ~~RF~~ ERF to AOD ratio, detailed in section 3 and discussed in section 4. Furthermore, our data, along with insights from previous studies, suggest that the ~~RF~~ ERF dependency on injected SO_2 identified by Niemeier and Timmreck (2015) acts as a lower boundary. Our conclusions are presented in section 5.

2 Method

2.1 Model

We use the CESM2 (Danabasoglu et al., 2020) in conjunction with the WACCM6 (Gettelman et al., 2019) and the fully dynamical ocean component Parallel Ocean Program version 2 (POP2) (R. Smith et al., 2010; Danabasoglu et al., 2020). The atmosphere model was run at a nominal 2° resolution with 70 vertical levels in the middle atmosphere (MA) configuration.

The WACCM6 version employed in the MA configuration uses the three mode version of the Modal Aerosol Module (MAM3) (Gettelman et al., 2019), a simplified and computationally efficient default setting within the Community Atmosphere Model version 5 (CAM5) (Liu et al., 2016), as described in Liu et al. (2012). The MAM3 was developed from MAM7 and features the modes Aitken, accumulation, and coarse (Liu et al., 2016), and further updated to simulate stratospheric sulfate aerosol from volcanic and non-volcanic emissions in WACCM (Mills et al., 2016).

2.2 Simulations

We are using the coupled model version BWma1850 component setup to run the CESM2 with a fully dynamic ocean component to get estimates of the GMST, and an accompanying fixed sea-surface temperature version, fSST1850, providing estimates of the ERF and AOD. The applied fSST1850 is not from a standardised component setup of CESM2 but is instead explicitly specified as `1850_CAM60%WCCM_CLM50%BGC-CROP_CICE%PRES_DOCN%DOM_MOSART_CISM2%NOEVOLVE_SWAV_TEST`. The component setup BWma1850 and fSST1850 differ in that the latter uses a prescribed sea-ice (`CICE -> CICE%PRES`), a prescribed data ocean (`POP2%ECO%DEP -> DOCN%DOM`) and a stub wave component instead of the full Wave Watch version 3 (`WW3 -> SWAV`).

The important input data used in the model simulations are injected SO_2 in units of teragrams ($Tg(SO_2)$), used to simulate volcanic eruptions. ERF is calculated as the combined (short wave and long wave) all-sky TOA energy imbalance, where the CESM2 provide the output variables "net solar flux at the top of the model" (FSNT) and "net longwave flux at the top of the model" (FLNT). Thus, $ERF_* = FSNT - FLNT$, and taking the difference between volcanic forcing simulations and a control simulation gives the final estimate of ERF ($ERF = ERF_{VOLC} - ERF_{CONTROL}$) (Marshall et al., 2020). The ERF calculation uses the fSST1850 component setup, which is also used to obtain all other simulation output fields except from GMST which uses BWma1850. The AOD is obtained from the output variable "stratospheric aerosol optical depth 550 nm day night" (AODVISstdn), while GMST is saved by CESM2 to the variable "reference height temperature" (TREFHT). The analysis of this work is performed using these four variables.

Appendix A provides a description of the simulation setup~~and utilised output variables~~. Table 1 summarises the simulations, encompassing four SO_2 injection magnitudes and up to four seasons: 15 February, 15 May, 15 August, and 15 November. The magnitudes vary over three orders of magnitude, or as introduced in Schmidt and Black (2022) across Volcano-Climate Index values 3 to 6: 26 $Tg(SO_2)$, 400 $Tg(SO_2)$, 1629 $Tg(SO_2)$, and 3000 $Tg(SO_2)$.

The smallest eruption case, ~~C2W↓~~S26, is similar in magnitude as compared to events like Mt. Pinatubo ($\sim$ 10–20 $Tg(SO_2)$; Timmreck et al., 2018) and Mt. Tambora ($\sim$ 56.2 $Tg(SO_2)$; Zanchettin et al., 2016). ~~($\sim$ 144–170 $Tg(SO_2)$; Vidal et al., 2016)~~ The intermediate case, S400, resembles the magnitude of the Samalas eruption in 1257 ($\sim$ 144–170 $Tg(SO_2)$; Vidal et al., 2016) however injecting about twice of the estimated SO_2, while the second largest and largest eruption cases, ~~C2W↑ and C2W↑↑~~S1629 and S3000, is in the likely range of the Young

Table 1. Simulations done with the CESM2[a]

Ensemble name	Tg(SO_2)	Lat [°N]	Lon [°E]	Alt [km]
~~C2W↑↑~~ S3000	3000	0	1	18–20
~~C2WN↑~~ S1629N	1629	56	287.7	18–20
~~C2W↑~~ S1629	1629	0	1	18–20
~~C2W−~~ S400	400	0	1	18–20
~~C2W↓~~ S26	26	0	1	18–20

~~[a]The ensembles C2WN↑ and C2W↑ have the same eruption magnitude, but while C2W↑ is located at the equator, C2WN↑ is located at a high northern latitude. C2W↑↑, C2W− and C2W↓ are located at the equator, but with different magnitudes compared to C2W↑. The three smallest tropical ensembles have four members, indicated by the number of eruption months, while the northern latitude and the extra large super-volcano ensemble consists of two members.~~

[a]The ensembles S1629 is located at the equat S26 are located at the three smallest in erupt by the number of erup members.

Toba Tuff (YTT) ~~eruption~~ supereruption occurring about 72 000 yr ago (100–10 000 Tg(SO_2); Jones et al., 2005). All eruptions were situated at the equator (0 °N, 1 °E) with SO_2 injected from 18 km to 20 km altitude with a linear ramp; 25% between 17.5 km and 18.5 km, 50% between 18.5 km and 19.5 km, and the last 25% between 19.5 km and 20.5 km. Collectively, the four tropical eruption cases ~~C2W↓, C2W−, C2W↑, and C2W↑↑~~ S26, S400, S1629, and S3000 are referred to as ~~C2WTrop~~STrop. An additional high-latitude eruption ensemble, labelled ~~C2WN↑~~S1629N, of the same injected SO_2 magnitude as ~~C2W↑~~ S1629 was simulated at 56 °N, 287.7 °E with a six-month separation (15 February and 15 August) between the two simulations.

3 Results

3.1 Analysis of the time series

Figure 1 presents time series of global mean AOD, ~~RF, and surface air temperature~~ERF, and GMST. The black lines represent the medians across the ensembles, while shading indicates the 5th to 95th percentiles. The four distinct forcing magnitudes (~~C2W↓, C2W−, C2W↑, and C2W↑↑~~S26, S400, S1629, and S3000) outlined in table 1 have been used. The time series in Fig. 1 are normalised by setting the peak value to unity, defined based on

the peak of a fit from a Savitzky-Golay filter of 3rd order and a one-year window length (Savitzky & Golay, 1964).

A notable feature across the subfigures of Fig. 1 is the peak occurrence of the ~~C2W↓~~ S26 case compared to the larger eruption cases. The peak of ~~C2W↓~~ S26 arrives earlier for both normalised AOD (Fig. 1a) and ~~temperature~~ normalised GMST (Fig. 1c), ~~.Cases C2W−, C2W↑, and C2W↑↑~~ while the normalised ERF time series in Fig. 1b are all indistinguishable. Cases S400, S1629, and S3000 are indistinguishable in their ~~temperature~~ normalised GMST development, and while ~~C2W↓~~ S26 peaks at an earlier time, it decays similarly to the other cases. Interestingly, the same development between ~~C2W− and C2W↑~~ S400 and S1629 is not found in the normalised AOD time series. ~~C2W↓~~ S26 peaks at an earlier time, but also spends more time around the peak and as such decays at a later time post-eruption. Likewise, ~~C2W−~~ S400 has a faster rise and slower decay compared to ~~C2W↑~~S1629, but where both peak at a similar time. ~~C2W↑ and C2W↑↑ have~~ S1629 and S3000 have similar normalised AOD developments, but where ~~C2W↑↑~~ S3000 show a slightly faster decay from the peak.

The timescale of the perturbation of AOD and ~~RF~~ ERF is shorter than that of the ~~temperature~~GMST. While the AOD and ~~RF~~ ERF time series return to their equilibrium state within roughly three years, the ~~temperature~~ GMST time series remain heavily perturbed three years post-eruption. Even when running the simulations for 20 years post-eruption, the ~~temperature~~ GMST time series are still decaying.

3.2 ~~RF~~ ERF dependency on AOD

We next focus on the development of the AOD and ~~RF~~ ERF time series relative to each other. Similar comparisons were conducted in Gregory et al. (2016, their Fig. 4) and Marshall et al. (2020, their Fig. 1), with ~~RF~~ ERF plotted against AOD. Figure 2 displays annual mean values from the five simulation cases in table 1; ~~the small eruption case (C2W↓)~~ S26 as blue downward-pointing triangles, ~~the intermediate eruption case (C2W−)~~ S400 as orange thick diamonds, ~~the large tropical eruption case (C2W↑)~~ S1629 as green upward-pointing triangles, ~~the extra large eruption case (C2W↑↑)~~ S3000 as small pink upward-pointing carets, and ~~the large northern hemisphere eruption case (C2WN↑)~~ S1629N as brown upward-pointing three-branched twigs. Also shown are the data from ~~Gregory et al. (2016, Fig. 4, black crosses from HadCM3 sstPiHistVol)~~ Gregory et al. (2016, Fig. 4, black crosses)

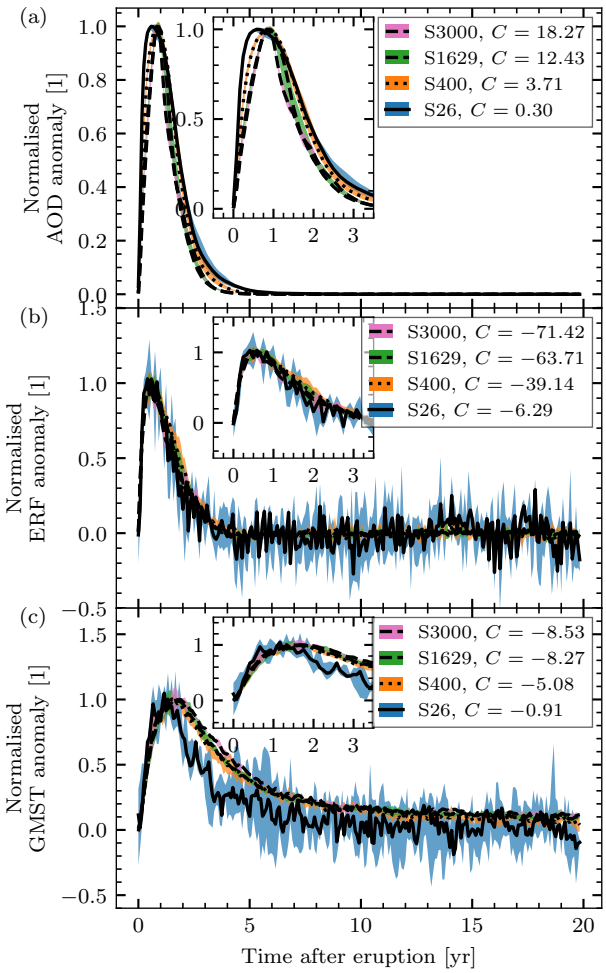

Figure 1. AOD (a), ~~RF~~ ERF (b) and ~~temperature~~ GMST response (c) time series to the four tropical volcanic eruption cases, ~~C2W↓~~S26, ~~C2W−~~S400, ~~C2W↑~~S1629, and ~~C2W↑↑~~S3000. The time series have been normalised to have peak values at unity, where C is the normalisation constant. Black lines indicate the median across the ensembles, while shading marks the 5th and 95th percentiles.

as grey crosses labelled G16 (described in Appendix B, section B3). Additionally, the estimated peak values from the Mt. Pinatubo and Mt. Tambora eruptions are plotted as a black star and plus, while the peak from the Jones et al. (2005) simulation is shown as a pink square labelled J05. Finally, red circles represent the peak values obtained from the ~~C2W~~ STrop eruption cases. The straight lines are the same as shown by Gregory et al. (2016). The full data range is shown in Fig. 2a while Fig. 2b highlights a narrow range, focusing on ~~the C2W↓ case~~S26.

The annual mean data from the Mt. Pinatubo-like ~~C2W↓~~ S26 case in Fig. 2b have ~~RF~~ ERF values as a function of AOD that follow almost the same constant slope as the G16 data. However, in Fig. 2a we observe that the stronger eruptions lead to dissimilar responses in AOD and ~~RF, where C2W−~~ ERF, where S400 seems to follow close to a -10 slope and ~~C2W↑~~ S1629 is closer to a -5 slope. The peak values (red circles) suggest a non-linear dependence, while within each eruption strength (same colour) the annual mean values fall relatively close to a straight line.

To investigate the time dependence of the ratio between ~~RF~~ ERF and AOD, we present seasonal means of this ratio in Fig. 3. The plot shows the eruption cases given in table 1, as well as the tropical eruptions from Marshall and Smith (2020) (6 of 82 eruptions), labelled M20 and described in Appendix B, section B2. The ~~C2W↑~~ S1629 case is similar to ~~C2W↑↑~~ S3000 as indicated in table 2, but is not shown in the plot to better highlight ~~C2WN↑~~S1629N. In Fig. 3a, lines are linear regression fits to the seasonal means across all ensemble members, summarised in table 2. Shaded regions are the standard deviation around the seasonal means. A similar ~~shading is plotted~~ plot is presented in Fig. 3b, but where the ~~regression fits have been omitted for clarity~~AOD and ERF time series were scaled to have peak values at unity before computing the ratio. As the AOD and ~~RF~~ ERF time series start from zero, the ratio from the first season is not included. Likewise, after three years both time series are almost fully equilibrated (Fig. 1a,b). The data is further divided into two periods; a pre-peak period where the peak of both the AOD and the ~~RF~~ ERF is included (consisting of the first post-eruption year), and a post-peak period for the decaying part (consisting of the second and third post-eruption years).

Although the ratio changes across the eruption magnitudes, we find that all the tropical cases follow a positive slope during the pre-peak period, as seen in Fig. 3a and described in table 2. The northern latitude case in ~~C2WN↑~~ S1629N shows a much flatter

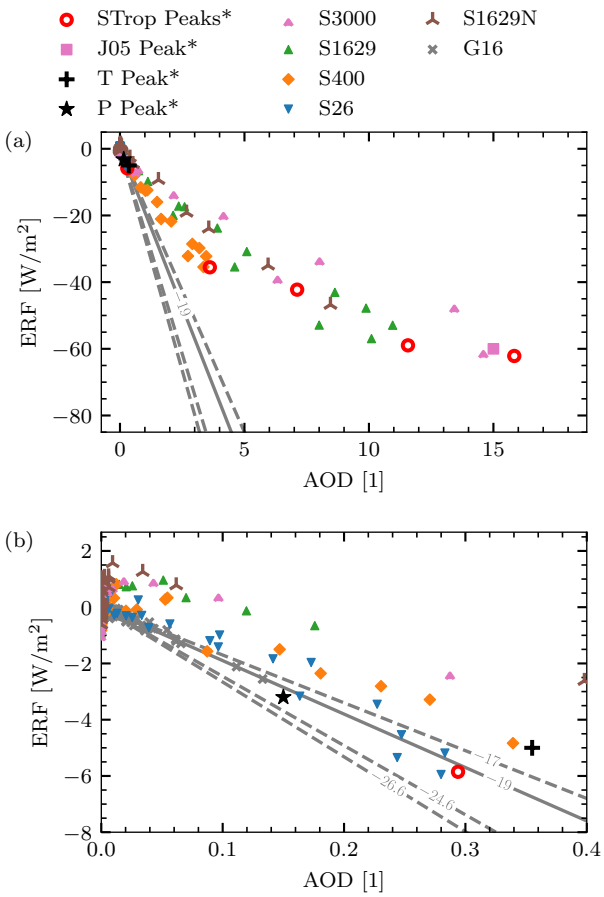

Figure 2. ~~RF~~ ERF as a function of AOD, yearly means. Data from the five simulations listed in table 1 (~~C2W↓~~S26, ~~C2W−~~S400, ~~C2W↑~~S1629, ~~C2WN↑~~S1629N, and ~~C2W↑↑~~S3000) are shown along with the data from the HadCM3 ~~sstPiHistVol~~ simulation by Gregory et al. (2016) (grey crosses, G16). Also shown are the estimated peak values of the Mt. Pinatubo (black star) and Mt. Tambora (black plus) eruptions. The peak values from the ~~C2W~~ STrop simulations are shown as red circles. Additionally in (a) the simulated super-volcano of Jones et al. (2005) (pink square) is shown. All peak values (as opposed to annual means) have an asterisk (∗) in their label. The grey lines are the same regression fits as in Gregory et al. (2016, Fig. 4), where the solid line is the fit to G16. (b): Zooming in on the smallest AOD values.

Table 2. Slope and standard deviation for the data in Fig. 3[a]

Figure	Ensemble name	Pre-peak	Post-peak
3a	~~C2WN↑~~ S1629N	0.45 ± 1.15	1.51 ± 1.45
	~~C2W↑↑~~ S3000	3.38 ± 0.97	-2.74 ± 0.77
	~~C2W↑~~ S1629	3.85 ± 0.52	-3.29 ± 0.60
	~~C2W—~~ S400	4.36 ± 0.82	-3.37 ± 0.59
	~~C2W↓~~ S26	3.64 ± 2.41	-1.41 ± 3.25
	M20	6.34 ± 1.77	-0.36 ± 1.33
3b	~~C2WN↑~~ S1629N	0.08 ± 0.20	0.27 ± 0.26
	~~C2W↑↑~~ S3000	0.86 ± 0.25	-0.70 ± 0.19
	~~C2W↑~~ S1629	0.75 ± 0.10	-0.64 ± 0.12
	~~C2W—~~ S400	0.43 ± 0.08	-0.34 ± 0.06
	~~C2W↓~~ S26	0.18 ± 0.12	-0.07 ± 0.16
	M20	0.33 ± 0.07	-0.02 ± 0.08

~~[a]The regression fits in the top half of the table are for Fig. 3a, while the bottom half is for Fig. 3b. The columns "pre-peak" and "post-peak" refer to the two periods as shown in Fig. 3. The ensembles are the same as those given in table 1, in addition to the 6 tropical eruptions from the 82 member ensemble in Marshall et al. (2020).~~

[a]The regression fits in
for Fig. 3a, while the
columns "pre-peak" a
periods as shown in F
same as those given in
tropical eruptions fro
Marshall et al. (2020).

slope compared to ~~C2WTrop~~ STrop and M20. The distinction between the slopes from the tropical and non-tropical cases is perhaps more clear in Fig. 3b and corresponding rows in table 2. Again, ~~C2WN↑~~ S1629N shows an almost flat slope compared to the tropical cases. During the post-peak period, more noise is introduced, but a weak tendency of negative slopes is found among the tropical cases, as well as in the ~~C2WN↑~~ S1629N case up to the last season where the noise is also the largest.

Marshall et al. (2020, their Fig. 1c,d) present results that demonstrate a time-dependent relationship in the conversion between AOD and ~~RF~~ERF. They obtain an ~~RF~~ ERF to AOD ratio with a negative slope when comparing the first post-eruption year to the second and third. As such, Marshall et al. (2020) find that, on average, the aerosol forcing

efficiency increases during the first two to three post-eruption years. This phenomenon is explained by Marshall et al. (2020) as the aerosols initially being spatially confined to the hemisphere where the eruption occurred. Subsequently, during the second and third years, they spread globally, resulting in a higher global-mean albedo per AOD and consequently a stronger ~~RF~~ ERF per AOD ratio with time. However, as noted above, a decrease in aerosol forcing efficiency is found when analysing the M20 data with seasonal resolution during the pre-peak period (first year post-eruption) while constraining the ensemble to only include eruptions within −10 to 10 °N. The post-peak period shows an increasing aerosol forcing efficiency, and during the full first three post-eruption years (pre-peak and post-peak), both the tropical subset and the full M20 data yield an increasing efficiency, as expected. Likewise, the first three post-eruption years of the ~~C2W−, C2W↑↑, and C2WN↑~~ S400, S3000, and S1629N cases show a weak negative slope and thus an increasing efficiency, while ~~C2W↓~~ S26 shows an elevated post-peak ratio as seen in Fig. 3b.

We also note that while the aerosol forcing efficiency is decreasing for tropical M20 data in the pre-peak period, the full dataset shows increasing efficiency. This is in line with what we find from ~~C2WN↑~~S1629N, which is the only eruption case that does not show a clear aerosol forcing efficiency decrease during the pre-peak period.

3.3 Parameter scan

In Fig. 4, we compare the peak values of all investigated CESM2 output parameters against each other as well as to injected SO_2~~. For our~~, grouped into tropical cases (~~C2WTrop),~~ STrop) and the high-latitude case (S1629N). We also include data from Marshall et al. (2020) (M20); Jones et al. (2005) (J05); Timmreck et al. (2010) (T10); English et al. (2013) (E13); Niemeier and Timmreck (2015) (N15); Otto-Bliesner et al. (2016) (OB16); Brenna et al. (2020) (B20); Osipov et al. (2020) (Os20); and McGraw et al. (2024) (McG24). A description of the climate models used is presented in table C1. Additionally, peak values from Mt. Pinatubo (P) and Mt. Tambora (T) are shown for reference.

For STrop, we observe in Fig. 4a an almost linear yet notably weakening relationship between AOD peak values and injected SO_2. The latitude also plays a role in the magnitude of the AOD perturbation, evident from ~~C2WN↑~~S1629N. This weak yet notable latitude dependence aligns with findings by Marshall et al. (2019), indicating that 72 % of the AOD variance can be attributed to injected SO_2, while latitude accounts for

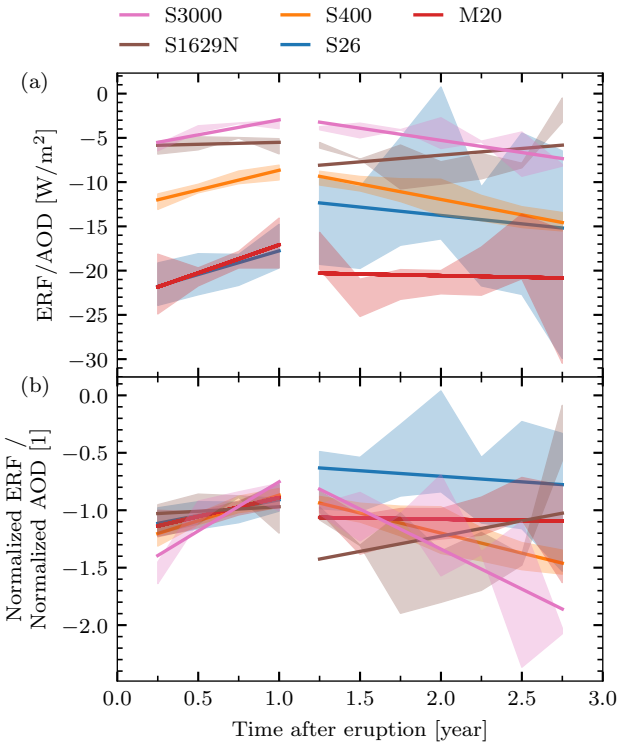

Figure 3. (a): The ratio of ~~RF~~ ERF to AOD, with time-after-eruption on the horizontal axis. Straight lines indicate linear regression fits and are described in table 2, while shaded regions are the standard deviation across the ensembles for each season. Regression fits and shadings are made for the pre-peak and post-peak periods. (b): Same as in (a), but where the underlying AOD and ~~RF~~ ERF time series have been scaled to have peak values at unity. Shown are data from table 1 along with tropical eruptions from M20. Values from each ensemble member is omitted for clarity, but we note that S26 include some outliers at positive ratio after the start of the second post-eruption year.

only 16 % of the variance. Peak values from their data (82 simulations) plotted as red thin diamonds display a similar pattern, with AOD exhibiting close to linear dependence on injected SO_2, but with latitude introducing a spread in AOD. Peak values from Mt. Pinatubo (P) and Mt. Tambora (T) ~~are shown for reference, along with~~ align well with simulation data, while peak values from ~~Jones et al. (2005) labelled~~ other simulations of large SO_2 magnitudes (J05~~and Timmreck et al. (2010) labelled~~ , E13, T10, Os20) show a larger spread, specifically to weaker AOD response. B20 align well with STrop, which also used the CESM2(WACCM6) climate model. Even though E13 used a similar yet simpler and older model in WACCM3 as compared to the CESM2(WACCM6) used by B20 and here, their AOD peak values are significantly smaller. However, E13 obtained significantly larger aerosols than B20; from an eruption injecting 2000 Tg(SO_2) E13 find a peak aerosol effective radius of $R_{\mathrm{EFF}} = 1.9\,\mu\mathrm{m}$, while B20 obtained $R_{\mathrm{EFF}} = 0.7\,\mu\mathrm{m}$ from an eruption injecting half as much SO_2. ~~The J05 is a simulation of a super-volcano based on a 100 times scaling of the AOD from Mt. Pinatubo, while T10 is a simulation of the YTT eruption based on SO_2injections.~~ Also shown is the two-thirds power-law relationship between AOD and injected SO_2 suggested by Crowley and Unterman (2013), scaled to yield the same value in AOD for an injection of 3000 Tg(SO_2) as obtained by S3000.

In Fig. 4b, ~~RF~~ ERF plotted against injected SO_2 (with the absolute value of ~~RF~~ ERF on the y-axis) ~~indicates a substantial damping effect on RF as injected SO_2increases for the C2W data~~ , show a sublinear ERF increase with increasing injected SO_2, in part due to the increase in aerosol effective radius with increasing eruption magnitudes (Timmreck et al., 2009) . This damping effect is seen in the STrop data to be in agreement with results from ~~Otto-Bliesner et al. (2016) , labelled OB16.~~ J05, B20, and McG24. While B20 uses the same climate model as STrop, McG24 uses the GISS ModelE2.1 but where a fixed aerosol effective radius of $R_{\mathrm{EFF}} = 0.6\,\mu\mathrm{m}$ was used. This R_{EFF} is at the lower end of their simulations, which is shown by McGraw et al. (2024) to produce the most extreme ERF and GMST perturbations. J05 used a third climate model in HadCM3, but simulates from the AOD estimate of Mt. Pinatubo multiplied by 100, and thus also assume small aerosol effective radius. The OB16 data come from a 2500 year long simulation using historic volcanoes as the only external forcing. The analysis details of OB16 can be found in Appendix B, section B1. Despite the model complexity difference as compared to STrop, Otto-Bliesner et al. (2016)'s simulations using Community Earth System Model version 1 (CESM1) with a low-top atmosphere (CAM5)

produce ~~RFs~~ ERFs comparable to our findings, also aligning well with the synthetic simulations of M20.

Niemeier and Timmreck (2015) conducted simulations of continuous sulphur injections up to 200 $\mathrm{Tg(SO_2)yr^{-1}}$ in the ECHAM5's middle atmosphere version (Giorgetta et al., 2006) with aerosol microphysics from HAM (Stier et al., 2005). They observed an ~~RF~~ ERF dependence on SO_2 injection rate following an inverse exponential, which converges to $-65\,\mathrm{Wm^{-2}}$, depicted in Fig. 4b as the stippled pink line labelled N15 and given as;

$$\Delta R_{\mathrm{TOA}}(x) = -65\,\mathrm{Wm^{-2}}\cancel{e^{-\left(\frac{2246\,\mathrm{Tg(S)yr^{-1}}}{x}\right)^{0.23}}}\exp\left[-\left(\frac{2246\,\mathrm{Tg(S)yr^{-1}}}{x}\right)^{0.23}\right]. \quad (1)$$

~~Both our simulations and OB16 exhibit a notably faster increase than this exponential relationship~~Here, x represents injected S per year in Tg, where injected mass in $\mathrm{Tg(SO_2)}$ is $2 \times \mathrm{Tg(S)}$. The results by N15, on which Eq. 1 is based, are all averages over at least three years of steady sulphur burdens, substantially longer than the time it takes for ~~RF~~ ERF to reach peak values after an eruption. Combined with their lack of a full chemistry model (Niemeier & Timmreck, 2015), a direct comparison between Eq. 1 to peak ~~RF~~ ERF values (occurring about one year post-eruption) may not reflect the same chemical and physical processes. ~~In Eq. 1, x represents S, while the axis shows values of SO_2, thus halving of the SO_2 values on the axis gives the appropriate shape of Eq. 1 as a function of S.~~

With these caveats in mind, we observe that even though most simulations exhibit a notably faster increase than the exponential relationship, T10's results closely align with the function described in Eq. 1. Starting with an initial input of 850 Tg(S) (equivalent to 1700 $\mathrm{Tg(SO_2)}$), representing the YTT eruption), their estimated AOD led to a peak ~~RF~~ ERF of $-18\,\mathrm{Wm^{-2}}$, depicted as a pink filled circle in Fig. 4b. The results from T10 came from a simulation using the MPI-ESM climate model, driven by AOD data from the HAM aerosol model. This alignment likely stems from the utilization of the same aerosol microphysical model in both Timmreck et al. (2010) and Niemeier and Timmreck (2015), as well as the application of similar climate models, MPI-ESM and ECHAM5, respectively. The relationship between climate model families and their implications are further described in Appendix C. Notably, the peak values from M20 align with OB16 and fit well within ~~an upper boundary defined by C2WTrop and OB16, and~~ a lower bound-

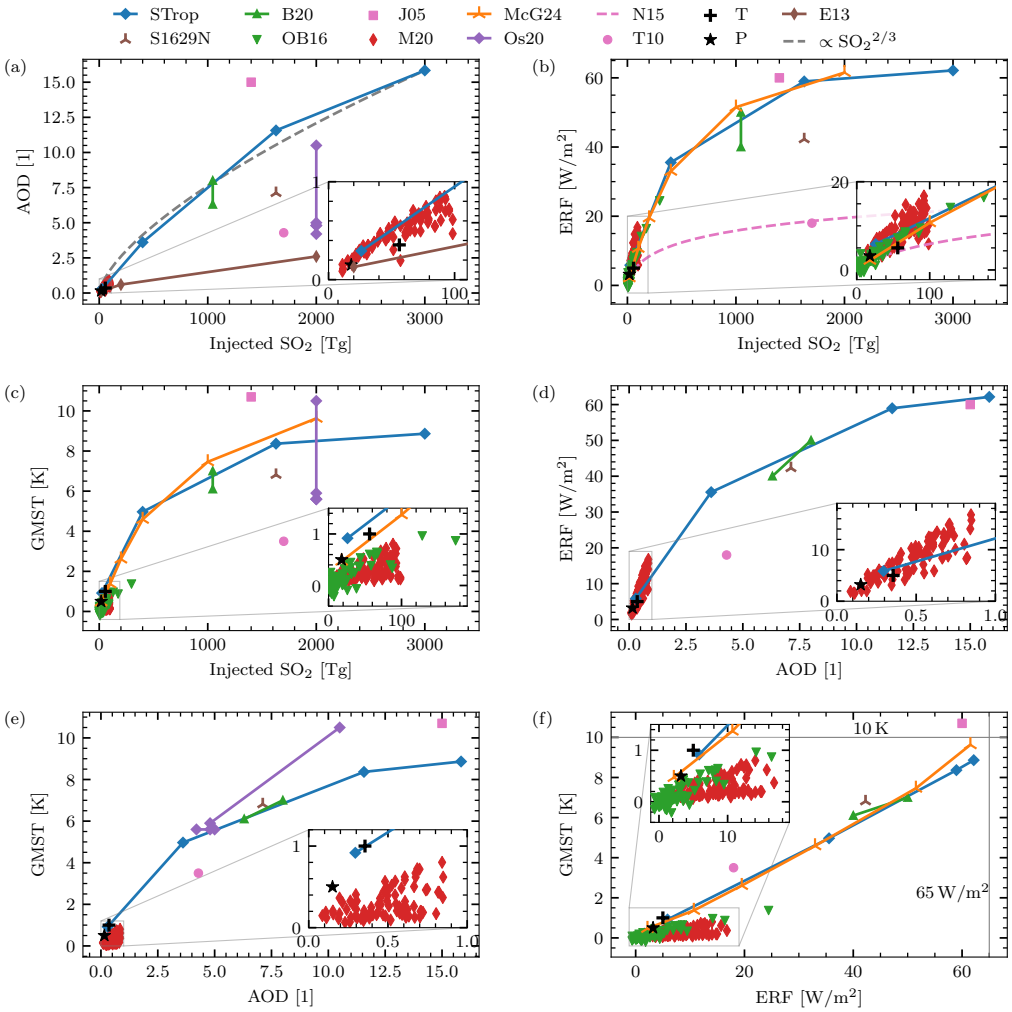

Figure 4. Peak values of (a) AOD, (b) ~~RF~~ERF, and (c) ~~temperature anomaly~~ GMST as a function of injected SO_2. (d) ~~RF~~ ERF and (e) ~~temperature anomaly~~ GMST as a function of AOD. (f) ~~Temperature anomaly~~ GMST as a function of ~~RF~~ERF. Blue diamonds labelled ~~C2WTrop~~ STrop represent tropical cases (~~C2W↓~~S26, ~~C2W—~~S400, ~~C2W↑~~S1629, ~~C2W↑↑~~S3000), the brown three-branched twig signifies the ~~C2WN↑~~ S1629N case, and green downward triangles denote OB16 ~~data from Otto-Bliesner et al. (2016)~~while green upward triangles denote B20. The pink square is J05 and the red thin diamonds ~~labelled~~ are M20~~display the Marshall and Smith (2020) data~~. McG24 and Os20 are indicated by purple upward twigs and orange diamonds, while pink circle and dashed line represent T10 and N15. Black star and plus indicate Mt. Pinatubo and Mt. Tambora estimates based on observations~~. The pink square labelled J05 refers to the one-hundred times Mt. Pinatubo super-volcano from Jones et al. (2005)~~ , and ~~the pink disk labelled T10 represents the YTT super-volcano from Timmreck et al. (2010)~~ brown thin diamonds denote E13. The ~~pink dashed~~ stippled grey line ~~labelled N15 is from Niemeier and Timmreck (2015), indicating~~ represent a two-thirds power-law relationship between AOD and SO_2 as suggested by Crowley and Unterman (2013). Note that all the ~~function~~ data points in ~~Eq~~the legend do not provide all four parameters, and are thus not part of every subfigure.~~ 1.~~

ary defined by Eq. 1. ~~Eruptions closer to the equator within M20 align with data points near the upper boundary, whereas eruptions at more extreme latitudes tend to yield weaker peak RF values, closer to the lower boundary.~~ Importantly, none of the eruption simulations shown in Fig. 4b exceeded the upper threshold of $-65\,\mathrm{Wm}^{-2}$ as suggested in Eq. 1.

Figure 4c illustrates the response of ~~temperature~~ GMST against injected SO_2. The increase in ~~temperature~~ GMST response with injected SO_2 decreases for higher injected SO_2, showing a similar relationship between ~~C2WTrop, C2WN↑, and~~ STrop, S1629N, OB16, B20, and McG24. Notably, T10 and J05 exhibit respectively much weaker and much stronger ~~temperature~~ GMST responses to injected SO_2 than ~~C2WTrop.~~ STrop, while Os20 cover a wide range in GMST for the same injceted SO_2 of 2000 Tg(SO_2). In Os20 they removed a single mechanism at the time, with four experiments with GMST between 5.5 K and 6 K, and one at ~ 10.5 K. For this outlier, feedback on photochemistry due to aerosols had been switched off (Osipov et al., 2020). T10 has a maximum ~~temperature~~ GMST anomaly of only -3.5 K for their 1700 Tg(SO_2) eruption, while J05 records a substantially larger maximum ~~temperature~~ GMST anomaly of -10.7 K. Since the M20 experiment was conducted with prescribed sea-surface temperatures (Marshall et al., 2020), preventing the ~~temperature~~ GMST from being fully perturbed, we do not focus on the M20 data in the GMST plots but include them for completeness.

In Fig. 4d, we revisit the relationship between ~~RF~~ ERF and AOD, focusing on peak values rather than annual and seasonal averages. As previously discussed, the ~~RF~~ ERF to AOD ratio displays weaker slopes than previous studies, with the ~~C2W~~ STrop peak values not conforming to a linear trend. The relationship between ~~RF~~ ERF and AOD suggests potential substantial dependencies on the model and its input parameters, such as latitude, but most notably to an inherent non-linear ~~RF~~ ERF dependence on AOD. Both the G16 data in Fig. 2 and the J05 data originate from the same climate model. Similarly to what we find from the ~~C2W~~ STrop data, the ratio is much stronger for small eruptions in the industrial era (G16) compared to the super-volcano eruption (J05).

In Fig. 4e, we again find that the response of the ~~C2WTrop data decreases with injected SO_2~~STrop data increases sublinearly with increasing AOD, this time in ~~temperature~~ GMST anomaly. Additionally, both ~~the C2WN↑ and the J05 cases~~ S1629N and B20 align well with ~~C2WTrop, with the~~ STrop, with T10~~case~~, and J05 and Os20 following a sim-

ilar dependence~~.~~, albeit somewhat weaker and stronger, respectively. We again note the one outlier from Os20 stemming from the simulation where feedback on photochemistry due to aerosols was switched off.

Finally, in Fig. 4f, we compare the ~~temperature and RF responses. Both C2WTrop and OB16 show a near-linear relationship between temperature and RF. The C2WTrop dataindicate a steeper slope~~ GMST and ERF responses. STrop show a remarkably linear relationship bewtween GMST and ERF, with most other simulations (S1629N, T10, B20, McG24) and observation based estimates (P, T) following STrop closely. J05 is also not far off the STrop data, but still represent a small deviation from the other estimates. OB16 also show a linear, yet shallower slope as compared to STrop, implying stronger ~~temperature perturbations~~ GMST perturbations in STrop as compared to OB16. However, potential biases exist in the values from the analysis of OB16, as outlined in Appendix B, section B1. This, along with considerable noise, results in the analysis of OB16 ~~temperature~~ GMST anomalies being less reliable. ~~As in Fig. 4c, the C2WN↑ case along with both the T10 and J05 cases closely follow the temperature to RF dependence of C2WTrop.~~

~~The almost linear relationship between AOD and injected SO_2 for the C2WTrop data in Fig. 4a suggests a comparable trend for RF versus injected SO_2 in Fig. 4b, as seen for RF versus AOD in Fig. 4d. For the same reason, we expect Fig. 4e to show a similar pattern for C2WTrop as observed in Fig. 4c.~~

~~This relationship, along with the functional relationships between all other parameters shown in Fig. 4, are illustrated in Fig. ??. There, , we must have that f, g, h, and k all have the same functional form, where $f : SO_2 \rightarrow RF$, $g : AOD \rightarrow T$, $h : SO_2 \rightarrow T$, and $k : AOD \rightarrow RF$. From this, we deduce that $f(x) = k(ax + b)$ and $h(x) = f(cx + d) = g(ax + b)$, and finally that $h(x) = k(acx + ad + b)$, concluding that f, g, h, and k have the same functional form.~~

~~Diagram describing the functional relationships of the parameters shown in Fig. 4.~~

3.4 Climate sensitivity estimate

As previously mentioned, the J05 experiment is similar to ~~C2W↑ concerning RF~~ S1629 concerning ERF values, yet differ in both AOD and ~~temperature~~GMST. At the same time J05 is similar to ~~C2W↑↑~~ S3000 in AOD and ~~RF~~ERF. To investigate this dis-

crepancy, we here conduct a comparison between the J05 climate feedback parameter α (where $s = 1/\alpha$ is the climate sensitivity parameter) with our climate resistance, denoted as ρ, and the transient climate response parameter (TCRP) $1/\rho$ (where TCS = $F_{2\times\mathrm{CO}_2} \times$ TCRP is the transient climate sensitivity and $F_{2\times\mathrm{CO}_2}$ is the forcing due to a doubling of pre-industrial CO_2 concentration). ~~, a duration too short~~ As the forcing of volcanic eruptions last for too short time for $F = \rho T$ to remain valid, an alternative approach using a time-integral form introduced by Merlis et al. (2014) is applied:

$$\int_0^\tau F \mathrm{d}t = \rho \int_0^\tau T \mathrm{d}t \tag{2}$$

$$\rho = \frac{\int_0^\tau F \mathrm{d}t}{\int_0^\tau T \mathrm{d}t}. \tag{3}$$

If the upper bound of the integral, τ, is sufficiently large, so that the upper ocean heat content is the same at $t = 0$ and $t = \tau$ (Merlis et al. (2014) used $\tau = 15\,\mathrm{yr}$), this approach agrees with $F = \rho T$ for long-term forcing (Gregory et al., 2016). Additionally, we note that the climate resistance and the climate feedback parameter are associated with the ocean heat uptake efficiency (κ) through $\rho = \alpha + \kappa$ (Gregory et al., 2016).

The climate feedback parameter estimated by Jones et al. (2005) is $\alpha \simeq 4\,\mathrm{Wm^{-2}K^{-1}}$, exceeding twice the value obtained by Gregory et al. (2016) in their simulations of Mt. Pinatubo using the same HadCM3 climate model. We determine the climate resistance using the integral-form computation outlined in Eq. 3 and adopting $\tau = 20\,\mathrm{yr}$. The estimated climate resistance from the three tropical simulation cases (with four in each ensemble) converges to $\rho = 2.5\pm0.4\,\mathrm{Wm^{-2}K^{-1}}$, and TCRP values of $1/\rho = 0.41\pm0.05\,\mathrm{KW^{-1}m^2}$, as reported in table 3, and is therefore assumed to be a good estimate of α.

Importantly, our estimate agrees well with G16, while the J05 estimate of $\alpha \simeq 4\,\mathrm{Wm^{-2}K^{-1}}$ is still notably higher. Since the ~~temperature~~ GMST perturbation obtained by J05 was larger than in any of our ~~CESM2~~ STrop cases, it indicates that the forcing used by J05 must be stronger. The peak value of the J05 ERF is similar to the S1629 case, and as such, the overall stronger forcing must originate from the development of the forcing time series rather than the peak value. This is in line with previous results showing that from larger eruptions, the aerosol effective radius peak increase, as well as the aerosol effective radius experiencing a shorter e-folding time (Clyne et al., 2021). This result in a sharper

Table 3. Estimated climate resistance and TCRP[a]

Simulation type	$\rho[\mathrm{Wm^{-2}K^{-1}}]$	$1/\rho$
~~C2W↑~~ S1629	2.21 ± 0.05	0.45 ± 0.01
~~C2W—~~ S400	2.51 ± 0.06	0.40 ± 0.01
~~C2W↓~~ S26	2.9 ± 0.6	0.36 ± 0.07
Total	2.5 ± 0.4	0.41 ± 0.05

~~[a]Estimates are based on ensembles with four members and $\tau = 20$ yr using Eq. 3.~~

[a]Estimates are based
members and $\tau = 20$ y

peak in AOD and ERF, with the peak values increasing sublinearly with increasing SO_2 (English et al., 2013; Timmreck et al., 2009; Zanchettin et al., 2016; Clyne et al., 2021) . In addition, OH scarcity is assumed to limit the SO_2 oxidation, delaying the AOD peak for sufficiently large eruptions (Timmreck et al., 2010). Further, McGraw et al. (2024) find that from supereruptions, it is possible to achieve even a warming of the GMST by fixing the aerosol effective radius to $R_{\mathrm{EFF}} > 2.5\,\mu\mathrm{m}$. As our model results align well with the results of McGraw et al. (2024) using a small aerosol effective radius of $R_{\mathrm{EFF}} = 0.6\,\mu\mathrm{m}$, we expect the peak GMST from CESM2(WACCM6) to be close to a lower (cooling) bound, and as such that the even colder GMST perturbation of Jones et al. (2005) is too extreme.

4 Discussion

Figures 2, 3, and 4d demonstrate that as the AOD exceeds approximately 1.0, the linear ~~RF~~ ERF dependence of approximately $-20\,\mathrm{Wm^{-2}AOD^{-1}}$ no longer holds. The sublinear increase in ~~RF~~ ERF with injected SO_2 in Fig. 4b for large eruptions is consistent with previous results from simulations using similar climate models of smaller historic eruptions (G16) and of ~~super-volcanoes~~ supereruptions (J05). Such a change in ratio has been attributed to larger eruptions, injecting more SO_2, leading to larger aerosols, and hence less effective radiation scattering, thereby reducing the ~~RF~~ ERF for the same injected SO_2 (English et al., 2013; Timmreck et al., 2010, 2018). Similarly, previous studies have suggested a two-thirds power law relationship between peek AOD and injected SO_2 for eruptions larger in magnitude than than the Mt. Tambora eruption (Crowley & Unterman, 2013; Metzner et a . Furthermore, CESM(WACCM) has been shown to simulate smaller aerosols than most

other climate models (Clyne et al., 2021), resulting in an increased AOD peak value and longer *e*-folding time (Zanchettin et al., 2016; Clyne et al., 2021). Thus, the sublinear relationship for AOD and ERF to injected SO_2 from CESM2(WACCM6) is likely an upper bound.

The non-linear relationship between peak ~~RF~~ ERF and AOD values is a strong signature in both Figs. 2 and 3. Across eruptions of the same strength, the ratio stays relatively constant, leading to a close to $-10\,\mathrm{Wm^{-2}AOD^{-1}}$ slope for ~~C2W−~~ S400 and a $-5\,\mathrm{Wm^{-2}AOD^{-1}}$ slope for ~~C2W↑ and C2W↑↑~~S1629 and S3000. Still, a non-linear development in the ~~RF~~ ERF to AOD ratio is found across all tropical eruptions. Similar to the results of Marshall et al. (2020), we find in ~~C2W−, C2W↑, and C2W↑↑~~ S400, S1629, and S3000 that the post-peak period (second and third post-eruption years) has a stronger aerosol forcing efficiency compared to the pre-peak period (first post-eruption year). The post-peak period of ~~C2W↓~~ S26 is elevated as compared to the pre-peak period, resulting in a decreasing aerosol forcing efficiency from the first to the second and third post-eruption years, in contrast to the other tropical eruptions.

Focusing on the pre-peak period, we find tropical eruptions to differ from eruptions at high latitudes. During the pre-peak period, all tropical eruptions show a decreasing aerosol forcing efficiency, while no significant change in the ~~RF~~ ERF to AOD ratio is found from the ~~C2WN↑~~ S1629N case. The full M20 dataset indicates an increasing aerosol forcing efficiency also during the pre-peak period, contrasting the decreasing efficiency found from their tropical eruptions and supporting the latitudinal dependence we find with ~~C2WN↑~~S1629N. While we find a linear relationship to be a useful approximation of ~~RF~~ ERF dependence on AOD for eruptions similar to or smaller than Mt. Pinatubo, additional factors must be considered for larger eruptions. These factors, such as OH scarcity contributing to delayed SO_2 oxidation, and aerosol growth ~~, influence~~ influencing reflectance and their gravitational pull, substantially ~~impacting~~ impact both AOD and ~~RF evolution, is~~ ERF evolution, as highlighted by Timmreck et al. (2010). The large difference in ratio found when comparing eruption magnitudes suggests that injected SO_2 is crucial when estimating the time-average of the ~~RF~~ ERF to AOD ratio. However, latitude and, in particular, aerosol dispersion are more influential in determining the post-eruption evolution of the ratio, particularly during the pre-peak period.

We find that the suggested upper threshold from Eq. 1 is not violated by any eruption simulation, and most notably that the ~~temperature~~ GMST peak value follow the ~~RF~~ ERF trend in reaching a limiting value. The ~~C2WTrop~~ STrop cases follow a close to linear ~~temperature dependency on RF, with the J05~~GMST dependency on ERF, with S1629N, T10, ~~and C2WN↑~~ B20, and McG24 all aligning close to the same slope. The linear relationship between ~~temperature and RF~~ GMST and ERF is the strongest dependence found between the parameters in Fig. 4, and a strong signature across both eruption magnitudes and latitudes, but also across highly different climate models. Thus, from a maximum ~~RF~~ ERF of $-65\,\mathrm{Wm}^{-2}$, we expect ~~temperature~~ GMST anomalies to reach at most ~~$\sim -12\,$K.~~ $\sim -10\,$K, in support of English et al. (2013) who suggested that large eruptions can be self-limiting. While J05 achieve an even stronger cooling, the long *e*-folding time of their AOD time series is believed to contribute a too strong forcing and climate feedback parameter, resulting in an estimated GMST that is too extreme.

The biggest spread in the data shown in Fig. 4 is found when relating injected SO_2 to any of the three output parameters. ~~As the amount of injected SO_2 increases, both~~ Computing the Pearson correlation coefficient for the data in Fig. 4 (except OB16 and M20, as they provide many more data points compared to all other and would skew the correlation) equates to 0.670, 0.799, and 0.758 for injected SO_2 against AOD, RF, and ~~temperature across models have a big spread.~~ GMST, respectively. In comparison, coefficients for AOD against ERF, AOD against GMST, and ERF against GMST equals 0.946, 0.918, and 0.986. The AOD to injected SO_2 relationship is consistent within similar models, even when comparing simulations of volcanic eruptions (Timmreck et al., 2010) and continuous injection of SO_2 (Niemeier & Timmreck, 2015), but has a wide spread at high values of injected SO_2 across model families (Figs. 4a,b,c). Comparatively, the ~~RF~~ ERF (Fig. 4d) and ~~temperature~~ GMST (Fig. 4e) as a function of AOD, as well as ~~temperature~~ GMST as a function of ~~RF~~ ERF (Fig. 4f), demonstrate a smaller spread across models. Marshall et al. (2019, 2020, 2021) use a code with seven log-normal modes to simulate aerosol mass and number concentrations, along with an atmosphere-only configuration of the UM-UKCA with prescribed sea-surface temperatures and sea-ice extent (Marshall et al., 2019). This approach is in contrast with CESM2, operating as an Earth System Model, but with a simpler aerosol chemistry model in the MAM3. The family of models to which M20 is based is different from that of ~~C2W and~~ STrop, OB16, ~~and also different from the~~ E13, and B20, with T10 and N15, and Os20 and McG24 from yet two more model

families, as described in Appendix C. Based on Fig. 4, we find the model family to be pivotal in determining the estimated AOD and ~~RF~~ ERF magnitudes from injected SO_2, whereas the various models generally demonstrate more consistency in representing ~~RF~~ ERF from AOD.

~~Timmreck et al. (2010) highlights that for sufficiently large eruptions, OH radicals are too scarce, which limits SO_2 oxidation. The AOD peak in the YTT simulation of T10 occurs six months after Mt. Pinatubo's peak. This aligns with our results, as illustrated in Fig. 1a, where C2W↓ shows an earlier AOD peak compared to C2W−, C2W↑, and C2W↑↑. While the peak RF value of T10 occurs 7–8 months post-eruption, similar to C2W, the J05 peak anomaly occurs one year post-eruption. Additionally, as Jones et al. (2005) obtains a climate feedback parameter larger than both what Gregory et al. (2016) found for the same climate model and larger than the climate resistance obtained here from C2W, we conclude that such a simple approach of scaling the AOD of smaller eruptions to represent larger eruptions is insufficient. Moreover, having a small ensemble of large eruptions to represent smaller eruptions is also insufficient when simulating from injected SO_2, as both AOD and temperature evolution are found to develop differently.~~

5 Summary and conclusions

We consider five ~~medium to super-volcano sized eruption ensembles~~ ensembles of Mt. Pinatubo-sized to supereruption sized events and compare them to previously reported results. We find the commonly adopted ~~RF~~ ERF dependence on AOD of $\sim -20\,\mathrm{Wm^{-2}AOD^{-1}}$ to be representative for Mt. Pinatubo-sized eruptions. Larger eruptions, with one to two orders of magnitude larger injections of SO_2, are found to have an ~~RF~~ ERF dependence on AOD closer to $\sim\ -10\,\mathrm{Wm^{-2}AOD^{-1}}$ and $\sim\ -5\,\mathrm{Wm^{-2}AOD^{-1}}$. A shallower slope for larger eruptions is also consistent with peak values from previous studies of ~~super-volcanoes~~supereruptions.

The time-after-eruption dependence of the ratio between ~~RF~~ ERF and AOD is found to weaken with time, resulting in a decreasing aerosol forcing efficiency in the pre-peak period. The effect is found across all eruption sizes, but only the tropical cases show a clear trend. The high-latitude case displays an almost constant efficiency with time. These results agree with a reanalysis of the tropical data in Marshall and Smith (2020). Thus, these findings provide strong supporting evidence that latitude is generally significant in determining the aerosol forcing efficiency, particularly as a function of time-after-eruption.

These findings emphasise the complexity of volcanic impacts on climate, demonstrating significant differences in climatic response depending on eruption magnitude and latitude.

A clear trend across all simulations performed here and across several previous studies is a linear relationship between peek GMST and ERF. Further, the peak values seem to stagnate with no ERF peaks breaking the suggested lower bound of ERF $= -65\,\mathrm{Wm}^{-2}$ by Niemeier and Timmreck (2015). Thus, we expect supereruptions to be self-limiting with the most extreme GMST perturbations reaching at most $\sim -10\,\mathrm{K}$.

We find that the AOD peak arrives later for larger eruptions than for smaller ones, and also that larger eruptions produce a sharper peak in the AOD time series. The ~~RF~~ ERF time series are similar across all eruption sizes, and while the smallest eruption experiences a faster ~~temperature~~ GMST decay, the larger eruptions produce time series indistinguishable in development for both ~~RF and temperature~~ERF and GMST. Thus, a simple scaling of the AOD or ~~temperature~~ GMST time series from a smaller eruption is insufficient in representing that of larger volcanic eruptions.

Considering injected SO_2 and the peak values of AOD and ~~RF~~ERF, a large spread is found across model families in Fig. 4. Improving the consistency between model families in how the chemistry and physics of ~~SO_2 and H_2SO_4~~ aerosols are represented is an important step in enhancing the accuracy of simulated volcanic eruptions' influence on climate by models. More simulations of larger volcanic eruptions with injected SO_2 greater than 200 Tg(SO2) would provide useful information for a more precise determination of the ~~RF~~ ERF to AOD ratio in the non-linear regime. This would also serve as a useful test to check if a comparison between SO_2 injection events and continuous SO_2 injection is reasonable. Introducing a spread in latitude similar to the Marshall and Smith (2020) dataset would allow for better comparison between eruptions across all latitudes and the suggested lower limit following Eq. 1, describing a situation of aerosol saturation.

Appendix A Simulation ~~set up and output~~setup

Input files used in the simulations were created by modifying the file available at `http://svn.code.sf.net/p/codescripts/code/trunk/ncl/emission/createVolcEruptV3.ncl`, using a Python package available on GitHub at `https://github.com/engeir/`

`volcano-cooking` or through the Python Package Index (PyPI). The package is available both as a library and a Command Line Interface (CLI), and is used to create volcanic eruptions with a specified amount of SO_2 that is injected over six hours at a given latitude, longitude, and altitude. All volcanic SO_2 files are created from a shell script by setting the eruption details in a JSON file that is read by the `volcano-cooking` CLI at a fixed version, ensuring a reproducible experiment setup.

~~We are using the coupled model version `BWma1850` component setup to run the CESM2, and an accompanying fixed sea-surface temperature version, `fSST1850`, to obtain estimates of the RF. The applied `fSST1850` is not from a standardised component setup but is instead explicitly specified as . The component setup `BWma1850` and `fSST1850` differ in that the latter uses a prescribed sea-ice (`CICE -> CICE%PRES`), a prescribed data ocean (`POP2%ECO%DEP -> DOCN%DOM`) and a stub wave component instead of the full Wave Watch version 3 (`WW3 -> SWAV`).~~

~~The important input data used in the model simulations are injected SO_2 in units of teragrams ($Tg(SO_2)$), used to simulate volcanic eruptions. RF is calculated as the combined (short wave and long wave) all-sky TOA energy imbalance, where the CESM2 provide the output variables "net solar flux at the top of the model" (FSNT) and "net longwave flux at the top of the model" (FLNT). Thus, $RF_* = FSNT - FLNT$, and taking the difference between volcanic forcing simulations and a control simulation gives the final estimate of RF ($RF = RF_{VOLC} - RF_{CONTROL}$) (Marshall et al., 2020). The RF calculation is based on `fSST1850`, hence this outline specifically describes how to calculate ERF as opposed to IRF, which instead is the difference between the ERF and the sum of all rapid atmospheric adjustments (Marshall et al., 2020; C. J. Smith et al., 2018). The AOD is obtained from the output variable "stratospheric aerosol optical depth 550 nm day nigth" (AODVISstdn), while global temperature is saved by CESM2 to the variable "reference height temperature" (TREFHT). The analysis of this work is performed using these four variables.~~

During analysis, one outlier was found in the ensemble representing ~~C2W↓~~S26, specifically in the ~~temperature~~ GMST time series. This ensemble member was the February 15, 1850, eruption, which was changed in ~~favor~~ favour of a February 15, 1851, eruption in the ~~C2W↓, C2W−, and C2W↑~~ S26, S400, and S1629 ensembles. For completeness, the February 15, 1850, eruption is still included in the online archive.

Appendix B External data

B1 Otto-Bliesner data analysis

Data from Otto-Bliesner et al. (2016) are the original input data of injected SO_2 as used in their model simulations, along with ~~RF and temperature~~ ERF and GMST output data. The injected SO_2 can be found at `https://www.cesm.ucar.edu/working-groups/paleo/simulations/ccsm4-lm`. Only the peak values of the SO_2 dataset were used in the analysis. Output variables are available at `www2.cesm.ucar.edu/models/experiments/LME`.

Since the OB16 dataset contains a five-member ensemble, the final ~~RF and temperature~~ ERF and GMST time series used were ensemble means. A single control simulation time series is used to remove seasonal dependence from the ~~temperature~~GMST, where the control simulation is averaged into a climatology mean. Further, a drift in the ~~temperature~~ GMST is removed by subtracting a linear regression fit. ~~RF~~ ERF has seasonality removed in the Fourier domain.

The time of an eruption is found based on a best attempt at aligning the SO_2 time series with both the ~~RF~~ ERF time series and the ~~temperature~~ GMST time series. The ~~RF and temperature~~ ERF and GMST peak values are taken as the value of the time series at the time of an eruption according to the SO_2 time series. Missing the true peak means the found peaks will be biased towards lower values. However, instances where eruptions occur close in time will contribute a bias to higher values. These biases contribute to a greater uncertainty related to OB16 in Figs. 4b,c,f.

B2 Marshall data analysis

Data used to compute the M20 values were from Marshall and Smith (2020), available at `https://doi.org/10.5285/232164e8b1444978a41f2acf8bbbfe91`. As each file includes a single eruption, peak values of AOD, ~~RF, and temperature~~ ERF, and GMST were found by applying a Savitzky-Golay filter of third order and one-year window length, and choosing the maximum value (Savitzky & Golay, 1964).

B3 Gregory data analysis

Data used to compute G16 values were kindly provided by Jonathan Gregory (personal communication). This include a 160-year long simulation with the HadCM3 using the sstPiHistVol simulation set-up, specifying a fixed sea-surface temperature simulation of historic volcanoes in pre-industrial conditions. The full 160-year-long time series were further analysed by computing annual means.

Appendix C Model families

The model used here was the CESM2 with the WACCM6 atmosphere in the MA configuration. The MA configuration uses the MAM3 (Gettelman et al., 2019), a simplified and computationally efficient default setting within the CAM5 (Liu et al., 2016), as described in Liu et al. (2012). The MAM3 was developed from MAM7, consisting of the seven modes Aitken, accumulation, primary carbon, fine dust, fine sea salt, coarse dust, and coarse sea salt. Instantaneous internal mixing of primary carbonaceous aerosols with secondary aerosols and instantaneous ageing of primary carbonaceous particles are assumed by emitting primary carbon in the accumulation mode (Liu et al., 2016). As dust absorbs water efficiently and is expected to be removed by wet deposition similarly to sea salt, fine dust is merged with fine sea salt into the accumulation mode and coarse dust is merged with coarse sea salt into a coarse mode. The coarse mode will quickly revert to its background state below the tropopause (Liu et al., 2012). Consequently, MAM3 features the three modes Aitken, accumulation, and coarse (Liu et al., 2016).

The CESM2 is an ancestor of CESM1 used by OB16. They belong to a different model family than both the HadCM3 (J05 and G16) and the UM-UKCA (M20), which is an extended version of HadGEM3 (Dhomse et al., 2014), and an ancestor of HadCM3. A third model family is represented through ECHAM5 (N15) and MPI-ESM (T10), where the latter is related to the former via the ECHAM6. Finally, a fourth family is represented through the GISS ModelE2.1 used by both Os20 and McG24. A summary of the model code genealogy is in table C1, based on the model code genealogy map created by Kuma et al. (2023).

Acronyms

AODVISstdn "stratospheric aerosol optical depth 550 nm day night"

Table C1. Model code family relations[a]

Family relation	Model name
CESM1 → CESM1-CAM5 → CESM2	CESM1
	CESM2
HadCM3 → HadGEM1 → HadGEM2 → HadGEM3 → UM-UKCA	HadCM3
	UM-UKCA
ECHAM5 → ECHAM6 → MPI-ESM	ECHAM5
	MPI-ESM
GISS-E2.1	GISS ModelE2.1

[a]~~Overview of various model codes grouped into families according to the model code genealogy map by Kuma et al. (2023), with each table entry also indicating the specific model code used in the referenced papers of this study.~~

[a]Overview of various m
genealogy map by Kum
model code used in th
WACCM3, only simul
OB16, B20 and this co

AOD stratospheric aerosol optical depth

CAM5 Community Atmosphere Model Version 5

CESM1 Community Earth System Model Version 1

CESM2 Community Earth System Model Version 2

ECS equilibrium climate sensitivity

ERF effective radiative forcing

FLNT "net longwave flux at the top of the model"

FSNT "net solar flux at the top of the model"

GMST global mean surface temperature

IRF instantaneous radiative forcing

MAM3 three mode version of the Modal Aerosol Module

MA middle atmosphere

POP2 Parallel Ocean Program Version 2

ERF effective radiative forcing

TCRP transient climate response parameter

TOA top-of-the-atmosphere

TREFHT "reference height temperature"

WACCM6 Whole Atmosphere Community Climate Model Version 6

YTT Young Toba Tuff

Open Research Section

The direct output data of CESM2 are too large to be easily archived and transferred. Instead, data generated directly from output fields of CESM2 are made available in a NIRD Research Data Archive ~~(?, ?)~~(Enger, 2024b), and were generated using scripts available at `https://github.com/engeir/cesm-data-aggregator`. Analysis scripts are available at GitHub (`https://github.com/engeir/code-to-radiative-forcing-by-super-volcano-eruptions`) and is published to Zenodo ~~(?, ?)~~(Enger, 2024a). Source code used to generate CESM2 input files are available at `https://github.com/engeir/cesm2-volcano-setup`.

Acknowledgments

The simulations were performed on resources provided by Sigma2 — the National Infrastructure for High Performance Computing and Data Storage in Norway.

This work was supported by the Tromsø Research Foundation under Grant Number 19_SG_AT.

Thanks to both Maria Rugenstein and Martin Rypdal for valuable discussions. We would also like to thank the authors of Gregory et al. (2016), Otto-Bliesner et al. (2016), and Marshall and Smith (2020) for making their data available.

References

Andersson, S. M., Martinsson, B. G., Vernier, J.-P., Friberg, J., Brenninkmeijer, C. A. M., Hermann, M., ... Zahn, A. (2015). Significant radiative impact of volcanic aerosol in the lowermost stratosphere. *Nature Communications*, *6*, 7692-. Retrieved from `https://doi.org/10.1038/ncomms8692` doi: 10.1038/ncomms8692

Bender, F. A. M., Ekman, A. M. L., & Rodhe, H. (2010, October). Response to the eruption of Mount Pinatubo in relation to climate sensitivity in the CMIP3 models. *Climate Dynamics*, *35*(5), 875–886. Retrieved

from http://link.springer.com/10.1007/s00382-010-0777-3 doi: 10.1007/s00382-010-0777-3

Boer, G. J., Stowasser, M., & Hamilton, K. (2007, February). Inferring climate sensitivity from volcanic events. *Climate Dynamics*, *28*(5), 481–502. Retrieved from http://link.springer.com/10.1007/s00382-006-0193-x doi: 10.1007/s00382-006-0193-x

Brenna, H., Kutterolf, S., Mills, M. J., & Krüger, K. (2020). The potential impacts of a sulfur- and halogen-rich supereruption such as los chocoyos on the atmosphere and climate. *Atmospheric Chemistry and Physics*, *20*(11), 6521–6539. Retrieved from https://acp.copernicus.org/articles/20/6521/2020/ doi: 10.5194/acp-20-6521-2020

Clyne, M., Lamarque, J.-F., Mills, M. J., Khodri, M., Ball, W., Bekki, S., ... Toon, O. B. (2021). Model physics and chemistry causing intermodel disagreement within the volmip-tambora interactive stratospheric aerosol ensemble. *Atmospheric Chemistry and Physics*, *21*(5), 3317–3343. Retrieved from https://acp.copernicus.org/articles/21/3317/2021/ doi: 10.5194/acp-21-3317-2021

Crowley, T. J., & Unterman, M. B. (2013). Technical details concerning development of a 1200 yr proxy index for global volcanism. *Earth System Science Data*, *5*(1), 187–197. Retrieved from https://essd.copernicus.org/articles/5/187/2013/ doi: 10.5194/essd-5-187-2013

Danabasoglu, G., Lamarque, J.-F., Bacmeister, J., Bailey, D. A., DuVivier, A. K., Edwards, J., ... Strand, W. G. (2020). The community earth system model version 2 (CESM2). *Journal of Advances in Modeling Earth Systems*, *12*(2), e2019MS001916. Retrieved from https://agupubs.onlinelibrary.wiley.com/doi/abs/10.1029/2019MS001916 (e2019MS001916 2019MS001916) doi: 10.1029/2019MS001916

Dhomse, S. S., Emmerson, K. M., Mann, G. W., Bellouin, N., Carslaw, K. S., Chipperfield, M. P., ... Thomason, L. W. (2014). Aerosol microphysics simulations of the mt. pinatubo eruption with the um-ukca composition-climate model. *Atmospheric Chemistry and Physics*, *14*(20), 11221–11246. Retrieved from https://acp.copernicus.org/articles/14/11221/2014/ doi: 10.5194/acp-14-11221-2014

Douglass, D. H., Knox, R. S., Pearson, B. D., & Jr., A. C. (2006). Thermocline flux exchange during the pinatubo event. *Geophysical Research Letters*, *33*(19), L19711. Retrieved from https://agupubs.onlinelibrary.wiley.com/doi/abs/10.1029/2006GL026355 doi: 10.1029/2006GL026355

Enger, E. R. (2024a, August). *Accompanying code to 'Radiative forcing by super-volcano eruptions'.* Zenodo. Retrieved from https://doi.org/10.5281/zenodo.13623401 doi: 10.5281/zenodo.13623401

Enger, E. R. (2024b). *CESM2(WACCM6) single super-volcano simulations* [Dataset]. Norstore. Retrieved from https://doi.org/10.11582/2024.00025 doi: 10.11582/2024.00025

English, J. M., Toon, O. B., & Mills, M. J. (2013). Microphysical simulations of large volcanic eruptions: Pinatubo and toba. *Journal of Geophysical Research: Atmospheres*, *118*(4), 1880–1895. Retrieved from https://agupubs.onlinelibrary.wiley.com/doi/abs/10.1002/jgrd.50196 doi: 10.1002/jgrd.50196

Forster, P. M., Richardson, T., Maycock, A. C., Smith, C. J., Samset, B. H., Myhre, G., ... Schulz, M. (2016). Recommendations for diagnosing effective radiative forcing from climate models for CMIP6. *Journal of Geophysical Research: Atmospheres*, *121*(20), 12,460–12,475. Retrieved from https://agupubs.onlinelibrary.wiley.com/doi/abs/10.1002/2016JD025320 doi: 10.1002/2016JD025320

Gettelman, A., Mills, M. J., Kinnison, D. E., Garcia, R. R., Smith, A. K., Marsh, D. R., ... Randel, W. J. (2019). The whole atmosphere community climate model version 6 (WACCM6). *Journal of Geophysical Research: Atmospheres*, *124*(23), 12380–12403. Retrieved from https://agupubs.onlinelibrary.wiley.com/doi/abs/10.1029/2019JD030943 doi: 10.1029/2019JD030943

Giorgetta, M. A., Manzini, E., Roeckner, E., Esch, M., & Bengtsson, L. (2006). Climatology and forcing of the quasi-biennial oscillation in the maecham5 model. *Journal of Climate*, *19*(16), 3882 - 3901. Retrieved from https://journals.ametsoc.org/view/journals/clim/19/16/jcli3830.1.xml doi: 10.1175/JCLI3830.1

Gregory, J. M., Andrews, T., Good, P., Mauritsen, T., & Forster, P. M. (2016, December 01). Small global-mean cooling due to volcanic radiative forcing. *Cli-*

mate Dynamics, *47*, 3979–3991. Retrieved from https://doi.org/10.1007/s00382-016-3055-1 doi: 10.1007/s00382-016-3055-1

Hansen, J., Nazarenko, L., Ruedy, R., Sato, M., Willis, J., Genio, A. D., ... Tausnev, N. (2005). Earth's energy imbalance: Confirmation and implications. *Science*, *308*(5727), 1431–1435. Retrieved from https://science.sciencemag.org/content/308/5727/1431 doi: 10.1126/science.1110252

Hansen, J., Sato, M., Ruedy, R., Nazarenko, L., Lacis, A., Schmidt, G. A., ... Zhang, S. (2005). Efficacy of climate forcings. *Journal of Geophysical Research: Atmospheres*, *110*(D18). Retrieved from https://agupubs.onlinelibrary.wiley.com/doi/abs/10.1029/2005JD005776 doi: 10.1029/2005JD005776

Jones, G. S., Gregory, J. M., Stott, P. A., Tett, S. F. B., & Thorpe, R. B. (2005, December 01). An AOGCM simulation of the climate response to a volcanic super-eruption. *Climate Dynamics*, *25*(7), 725–738. Retrieved from https://doi.org/10.1007/s00382-005-0066-8 doi: 10.1007/s00382-005-0066-8

Kuma, P., Bender, F. A.-M., & Jönsson, A. R. (2023). Climate model code genealogy and its relation to climate feedbacks and sensitivity. *Journal of Advances in Modeling Earth Systems*, *15*(7), e2022MS003588. Retrieved from https://agupubs.onlinelibrary.wiley.com/doi/abs/10.1029/2022MS003588 (e2022MS003588 2022MS003588) doi: 10.1029/2022MS003588

Liu, X., Easter, R. C., Ghan, S. J., Zaveri, R., Rasch, P., Shi, X., ... Mitchell, D. (2012). Toward a minimal representation of aerosols in climate models: description and evaluation in the community atmosphere model CAM5. *Geoscientific Model Development*, *5*(3), 709–739. Retrieved from https://gmd.copernicus.org/articles/5/709/2012/ doi: 10.5194/gmd-5-709-2012

Liu, X., Ma, P.-L., Wang, H., Tilmes, S., Singh, B., Easter, R. C., ... Rasch, P. J. (2016). Description and evaluation of a new four-mode version of the modal aerosol module (MAM4) within version 5.3 of the community atmosphere model. *Geoscientific Model Development*, *9*(2), 505–522. Retrieved from https://gmd.copernicus.org/articles/9/505/2016/ doi: 10.5194/gmd-9-505-2016

Marshall, L. R., Johnson, J. S., Mann, G. W., Lee, L., Dhomse, S. S., Regayre, L., ... Schmidt, A. (2019). Exploring how eruption source parameters affect volcanic radiative forcing using statistical emulation. *Journal of Geo-*

physical Research: Atmospheres, *124*(2), 964–985. Retrieved from https://agupubs.onlinelibrary.wiley.com/doi/abs/10.1029/2018JD028675 doi: 10.1029/2018JD028675

Marshall, L. R., Maters, E. C., Schmidt, A., Timmreck, C., Robock, A., & Toohey, M. (2022, May 04). Volcanic effects on climate: recent advances and future avenues. *Bulletin of Volcanology*, *84*(5), 54. Retrieved from https://doi.org/10.1007/s00445-022-01559-3 doi: 10.1007/s00445-022-01559-3

Marshall, L. R., Schmidt, A., Johnson, J. S., Mann, G. W., Lee, L. A., Rigby, R., & Carslaw, K. S. (2021). Unknown eruption source parameters cause large uncertainty in historical volcanic radiative forcing reconstructions. *Journal of Geophysical Research: Atmospheres*, *126*(13), e2020JD033578. Retrieved from https://agupubs.onlinelibrary.wiley.com/doi/abs/10.1029/2020JD033578 (e2020JD033578 2020JD033578) doi: 10.1029/2020JD033578

Marshall, L. R., & Smith, C. J. (2020, September 25). Vol-Clim: UM-UKCA interactive stratospheric aerosol model summary data for perturbed parameter ensemble of volcanic eruptions. *Centre for Environmental Data Analysis*. Retrieved from https://dx.doi.org/10.5285/232164e8b1444978a41f2acf8bbbfe91 doi: 10.5285/232164e8b1444978a41f2acf8bbbfe91

Marshall, L. R., Smith, C. J., Forster, P. M., Aubry, T. J., Andrews, T., & Schmidt, A. (2020). Large variations in volcanic aerosol forcing efficiency due to eruption source parameters and rapid adjustments. *Geophysical Research Letters*, *47*(19), e2020GL090241. Retrieved from https://agupubs.onlinelibrary.wiley.com/doi/abs/10.1029/2020GL090241 (e2020GL090241 2020GL090241) doi: 10.1029/2020GL090241

Marvel, K., Schmidt, G. A., Miller, R. L., & Nazarenko, L. S. (2016, April 01). Implications for climate sensitivity from the response to individual forcings. *Nature Climate Change*, *6*(4), 386–389. Retrieved from https://doi.org/10.1038/nclimate2888 doi: 10.1038/nclimate2888

McGraw, Z., DallaSanta, K., Polvani, L. M., Tsigaridis, K., Orbe, C., & Bauer, S. E. (2024). Severe global cooling after volcanic super-eruptions? the answer hinges on unknown aerosol size. *Journal of Climate*, *37*(4), 1449 - 1464. Retrieved from https://journals.ametsoc.org/view/journals/clim/37/4/

JCLI-D-23-0116.1.xml doi: 10.1175/JCLI-D-23-0116.1

Merlis, T. M., Held, I. M., Stenchikov, G. L., Zeng, F., & Horowitz, L. W. (2014). Constraining transient climate sensitivity using coupled climate model simulations of volcanic eruptions. *Journal of Climate*, *27*(20), 7781–7795. Retrieved from https://journals.ametsoc.org/view/journals/clim/27/20/jcli-d-14-00214.1.xml doi: 10.1175/JCLI-D-14-00214.1

Metzner, D., Kutterolf, S., Toohey, M., Timmreck, C., Niemeier, U., Freundt, A., & Krüger, K. (2014). Radiative forcing and climate impact resulting from so2 injections based on a 200,000-year record of plinian eruptions along the central american volcanic arc. *International Journal of Earth Sciences*, *103*, 2063-2079. Retrieved from https://doi.org/10.1007/s00531-012-0814-z doi: 10.1007/s00531-012-0814-z

Mills, M. J., Richter, J. H., Tilmes, S., Kravitz, B., MacMartin, D. G., Glanville, A. A., ... Kinnison, D. E. (2017). Radiative and chemical response to interactive stratospheric sulfate aerosols in fully coupled CESM1(WACCM). *Journal of Geophysical Research: Atmospheres*, *122*(23), 13,061–13,078. Retrieved from https://agupubs.onlinelibrary.wiley.com/doi/abs/10.1002/2017JD027006 doi: 10.1002/2017JD027006

Mills, M. J., Schmidt, A., Easter, R., Solomon, S., Kinnison, D. E., Ghan, S. J., ... Gettelman, A. (2016). Global volcanic aerosol properties derived from emissions, 1990–2014, using CESM1(WACCM). *Journal of Geophysical Research: Atmospheres*, *121*(5), 2332–2348. Retrieved from https://agupubs.onlinelibrary.wiley.com/doi/abs/10.1002/2015JD024290 doi: 10.1002/2015JD024290

Myhre, G., Shindell, D., Bréon, F.-M., Collins, W., Fuglestvedt, J., Huang, J., ... Zhang, H. (2013). Anthropogenic and natural radiative forcing. In T. F. Stocker et al. (Eds.), *Climate change 2013: The physical science basis. contribution of working group i to the fifth assessment report of the intergovernmental panel on climate change* (pp. 659–740). Cambridge, UK: Cambridge University Press. doi: 10.1017/CBO9781107415324.018

Niemeier, U., & Timmreck, C. (2015, August). What is the limit of climate engineering by stratospheric injection of so_2? *Atmospheric Chemistry and Physics*, *15*(16), 9129–9141. Retrieved from https://doi.org/

10.5194%2Facp-15-9129-2015 doi: 10.5194/acp-15-9129-2015

Ollila, A. (2016, 02). Climate sensitivity parameter in the test of the mount pinatubo eruption. *Physical Science International Journal,*, *9*, 1–14. doi: 10.9734/PSIJ/2016/23242

Osipov, S., Stenchikov, G., Tsigaridis, K., LeGrande, A. N., & Bauer, S. E. (2020). The role of the so radiative effect in sustaining the volcanic winter and soothing the toba impact on climate. *Journal of Geophysical Research: Atmospheres*, *125*(2), e2019JD031726. Retrieved from https://agupubs.onlinelibrary.wiley.com/doi/abs/10.1029/2019JD031726 (e2019JD031726 10.1029/2019JD031726) doi: 10.1029/2019JD031726

Otto-Bliesner, B. L., Brady, E. C., Fasullo, J., Jahn, A., Landrum, L., Stevenson, S., ... Strand, G. (2016). Climate variability and change since 850 CE: An ensemble approach with the community earth system model. *Bulletin of the American Meteorological Society*, *97*(5), 735–754. Retrieved from https://journals.ametsoc.org/view/journals/bams/97/5/bams-d-14-00233.1.xml doi: 10.1175/BAMS-D-14-00233.1

Pauling, A. G., Bitz, C. M., & Armour, K. C. (2023). The climate response to the mt. pinatubo eruption does not constrain climate sensitivity. *Geophysical Research Letters*, *50*(7), e2023GL102946. Retrieved from https://agupubs.onlinelibrary.wiley.com/doi/abs/10.1029/2023GL102946 (e2023GL102946 2023GL102946) doi: 10.1029/2023GL102946

Pinto, J. P., Turco, R. P., & Toon, O. B. (1989). Self-limiting physical and chemical effects in volcanic eruption clouds. *Journal of Geophysical Research: Atmospheres*, *94*(D8), 11165-11174. Retrieved from https://agupubs.onlinelibrary.wiley.com/doi/abs/10.1029/JD094iD08p11165 doi: https://doi.org/10.1029/JD094iD08p11165

Pitari, G., Genova, G. D., Mancini, E., Visioni, D., Gandolfi, I., & Cionni, I. (2016). Stratospheric aerosols from major volcanic eruptions: A composition-climate model study of the aerosol cloud dispersal and e-folding time. *Atmosphere*, *7*(6). Retrieved from https://www.mdpi.com/2073-4433/7/6/75 doi: 10.3390/atmos7060075

Rampino, M. R., & Self, S. (1982). Historic eruptions of tambora (1815), krakatau (1883), and agung (1963), their stratospheric aerosols, and cli-

matic impact. *Quaternary Research*, *18*(2), 127-143. Retrieved from https://www.sciencedirect.com/science/article/pii/0033589482900655 doi: https://doi.org/10.1016/0033-5894(82)90065-5

Richardson, T. B., Forster, P. M., Smith, C. J., Maycock, A. C., Wood, T., Andrews, T., ... Watson-Parris, D. (2019). Efficacy of Climate Forcings in PDRMIP Models. *Journal of Geophysical Research: Atmospheres*, *124*(23), 12824–12844. Retrieved from https://agupubs.onlinelibrary.wiley.com/doi/abs/10.1029/2019JD030581 doi: 10.1029/2019JD030581

Robock, A. (2000). Volcanic eruptions and climate. *Reviews of Geophysics*, *38*(2), 191–219. Retrieved from https://agupubs.onlinelibrary.wiley.com/doi/abs/10.1029/1998RG000054 doi: 10.1029/1998RG000054

Salvi, P., Ceppi, P., & Gregory, J. M. (2022). Interpreting differences in radiative feedbacks from aerosols versus greenhouse gases. *Geophysical Research Letters*, *49*(8), e2022GL097766. Retrieved from https://agupubs.onlinelibrary.wiley.com/doi/abs/10.1029/2022GL097766 (e2022GL097766 2022GL097766) doi: 10.1029/2022GL097766

Savitzky, A., & Golay, M. J. E. (1964). Smoothing and differentiation of data by simplified least squares procedures. *Analytical Chemistry*, *36*(8), 1627-1639. Retrieved from https://doi.org/10.1021/ac60214a047 doi: 10.1021/ac60214a047

Schmidt, A., & Black, B. A. (2022). Reckoning with the rocky relationship between eruption size and climate response: Toward a volcano-climate index [Journal Article]. *Annual Review of Earth and Planetary Sciences*, *50*(Volume 50, 2022), 627-661. Retrieved from https://www.annualreviews.org/content/journals/10.1146/annurev-earth-080921-052816 doi: 10.1146/annurev-earth-080921-052816

Schneider, D. P., Ammann, C. M., Otto-Bliesner, B. L., & Kaufman, D. S. (2009). Climate response to large, high-latitude and low-latitude volcanic eruptions in the community climate system model. *Journal of Geophysical Research: Atmospheres*, *114*(D15). Retrieved from https://agupubs.onlinelibrary.wiley.com/doi/abs/10.1029/2008JD011222 doi: 10.1029/2008JD011222

Schurer, A. P., Hegerl, G. C., Mann, M. E., Tett, S. F. B., & Phipps, S. J. (2013). Separating Forced from Chaotic Climate Variability over the Past Millennium.

Journal of Climate, *26*(18), 6954 - 6973. Retrieved from https://journals.ametsoc.org/view/journals/clim/26/18/jcli-d-12-00826.1.xml doi: 10.1175/JCLI-D-12-00826.1

Sigl, M., Toohey, M., McConnell, J. R., Cole-Dai, J., & Severi, M. (2022). Volcanic stratospheric sulfur injections and aerosol optical depth during the holocene (past 11 500 years) from a bipolar ice-core array. *Earth System Science Data*, *14*(7), 3167–3196. Retrieved from https://essd.copernicus.org/articles/14/3167/2022/ doi: 10.5194/essd-14-3167-2022

Smith, C. J., Kramer, R. J., Myhre, G., Forster, P. M., Soden, B. J., Andrews, T., ... Watson-Parris, D. (2018). Understanding rapid adjustments to diverse forcing agents. *Geophysical Research Letters*, *45*(21), 12,023–12,031. Retrieved from https://agupubs.onlinelibrary.wiley.com/doi/abs/10.1029/2018GL079826 doi: 10.1029/2018GL079826

Smith, R., Jones, P., Briegleb, B., Bryan, F., Danabasoglu, G., Dennis, J., ... Yeager, S. (2010, 03 23). The parallel ocean program (POP) reference manual. *LAUR-10-01853*. Retrieved from https://www.cesm.ucar.edu/models/cesm1.0/pop2/doc/sci/POPRefManual.pdf

Solomon, S., Daniel, J. S., Neely, R. R., Vernier, J.-P., Dutton, E. G., & Thomason, L. W. (2011). The persistently variable "background" stratospheric aerosol layer and global climate change. *Science*, *333*(6044), 866-870. Retrieved from https://www.science.org/doi/abs/10.1126/science.1206027 doi: 10.1126/science.1206027

Stier, P., Feichter, J., Kinne, S., Kloster, S., Vignati, E., Wilson, J., ... Petzold, A. (2005). The aerosol-climate model echam5-ham. *Atmospheric Chemistry and Physics*, *5*(4), 1125–1156. Retrieved from https://acp.copernicus.org/articles/5/1125/2005/ doi: 10.5194/acp-5-1125-2005

Timmreck, C., Graf, H.-F., Lorenz, S. J., Niemeier, U., Zanchettin, D., Matei, D., ... Crowley, T. J. (2010). Aerosol size confines climate response to volcanic supereruptions. *Geophysical Research Letters*, *37*(24). Retrieved from https://agupubs.onlinelibrary.wiley.com/doi/abs/10.1029/2010GL045464 doi: 10.1029/2010GL045464

Timmreck, C., Lorenz, S. J., Crowley, T. J., Kinne, S., Raddatz, T. J., Thomas, M. A., & Jungclaus, J. H. (2009). Limited temperature response to the

very large AD 1258 volcanic eruption. *Geophysical Research Letters*, *36*(21). Retrieved from https://agupubs.onlinelibrary.wiley.com/doi/abs/10.1029/2009GL040083 doi: 10.1029/2009GL040083

Timmreck, C., Mann, G. W., Aquila, V., Hommel, R., Lee, L. A., Schmidt, A., ... Weisenstein, D. (2018). The interactive stratospheric aerosol model intercomparison project (ISA-MIP): motivation and experimental design. *Geoscientific Model Development*, *11*(7), 2581–2608. Retrieved from https://gmd.copernicus.org/articles/11/2581/2018/ doi: 10.5194/gmd-11-2581-2018

Timmreck, C., Olonscheck, D., Ballinger, A. P., D'Agostino, R., Fang, S.-W., Schurer, A. P., & Hegerl, G. C. (2024). Linearity of the Climate Response to Increasingly Strong Tropical Volcanic Eruptions in a Large Ensemble Framework. *Journal of Climate*, *37*(8), 2455 - 2470. Retrieved from https://journals.ametsoc.org/view/journals/clim/37/8/JCLI-D-23-0408.1.xml doi: 10.1175/JCLI-D-23-0408.1

Toohey, M., Krüger, K., Niemeier, U., & Timmreck, C. (2011). The influence of eruption season on the global aerosol evolution and radiative impact of tropical volcanic eruptions. *Atmospheric Chemistry and Physics*, *11*(23), 12351–12367. Retrieved from https://acp.copernicus.org/articles/11/12351/2011/ doi: 10.5194/acp-11-12351-2011

Toohey, M., Krüger, K., Schmidt, H., Timmreck, C., Sigl, M., Stoffel, M., & Wilson, R. (2019, February 01). Disproportionately strong climate forcing from extratropical explosive volcanic eruptions. *Nature Geoscience*, *12*(2), 100–107. Retrieved from https://doi.org/10.1038/s41561-018-0286-2 doi: 10.1038/s41561-018-0286-2

Vidal, C. M., Métrich, N., Komorowski, J.-C., Pratomo, I., Michel, A., Kartadinata, N., ... Lavigne, F. (2016, October). The 1257 samalas eruption (lombok, indonesia): the single greatest stratospheric gas release of the common era. *Scientific Reports*, *6*(1). Retrieved from http://dx.doi.org/10.1038/srep34868 doi: 10.1038/srep34868

Wigley, T. M. L., Ammann, C. M., Santer, B. D., & Raper, S. C. B. (2005). Effect of climate sensitivity on the response to volcanic forcing. *Journal of Geophysical Research: Atmospheres*, *110*(D9). Retrieved from https://agupubs

.onlinelibrary.wiley.com/doi/abs/10.1029/2004JD005557 doi: 10.1029/2004JD005557

Zanchettin, D., Khodri, M., Timmreck, C., Toohey, M., Schmidt, A., Gerber, E. P., ... Tummon, F. (2016). The model intercomparison project on the climatic response to volcanic forcing (volMIP): experimental design and forcing input data for CMIP6. *Geoscientific Model Development*, *9*(8), 2701–2719. Retrieved from https://gmd.copernicus.org/articles/9/2701/2016/ doi: 10.5194/gmd-9-2701-2016

Zanchettin, D., Timmreck, C., Toohey, M., Jungclaus, J. H., Bittner, M., Lorenz, S. J., & Rubino, A. (2019). Clarifying the relative role of forcing uncertainties and initial-condition unknowns in spreading the climate response to volcanic eruptions. *Geophysical Research Letters*, *46*(3), 1602–1611. Retrieved from https://agupubs.onlinelibrary.wiley.com/doi/abs/10.1029/2018GL081018 doi: 10.1029/2018GL081018

Zhao, J., Turco, R. P., & Toon, O. B. (1995). A model simulation of pinatubo volcanic aerosols in the stratosphere. *Journal of Geophysical Research: Atmospheres*, *100*(D4), 7315-7328. Retrieved from https://agupubs.onlinelibrary.wiley.com/doi/abs/10.1029/94JD03325 doi: 10.1029/94JD03325

Zhuo, Z., Fuglestvedt, H. F., Toohey, M., & Krüger, K. (2024). Initial atmospheric conditions control transport of volcanic volatiles, forcing and impacts. *Atmospheric Chemistry and Physics*, *24*(10), 6233–6249. Retrieved from https://acp.copernicus.org/articles/24/6233/2024/ doi: 10.5194/acp-24-6233-2024